In situ solid-state electrochemistry of mass-selected ions at well-defined electrode–electrolyte interfaces

Venkateshkumar Prabhakaran[a], Grant E. Johnson[a], Bingbing Wang[b,1], and Julia Laskin[a,2]

[a]Physical Sciences Division, Pacific Northwest National Laboratory, Richland, WA 99352; and [b]Environmental Molecular Sciences Laboratory, Pacific Northwest National Laboratory, Richland, WA 99352

Edited by R. Graham Cooks, Purdue University, West Lafayette, IN, and approved October 10, 2016 (received for review May 31, 2016)

Molecular-level understanding of electrochemical processes occurring at electrode–electrolyte interfaces (EEIs) is key to the rational development of high-performance and sustainable electrochemical technologies. This article reports the development and application of solid-state in situ thin-film electrochemical cells to explore redox and catalytic processes occurring at well-defined EEIs generated using soft-landing (SL) of mass- and charge-selected cluster ions. In situ cells with excellent mass-transfer properties are fabricated using carefully designed nanoporous ionic liquid membranes. SL enables deposition of pure active species that are not obtainable with other techniques onto electrode surfaces with precise control over charge state, composition, and kinetic energy. SL is, therefore, demonstrated to be a unique tool for studying fundamental processes occurring at EEIs. Using an aprotic cell, the effect of charge state ($PMo_{12}O_{40}^{3-/2-}$) and the contribution of building blocks of Keggin polyoxometalate (POM) clusters to redox processes are characterized by populating EEIs with POM anions generated by electrospray ionization and gas-phase dissociation. Additionally, a proton-conducting cell has been developed to characterize the oxygen reduction activity of bare Pt clusters (Pt_{30} ~1 nm diameter), thus demonstrating the capability of the cell for probing catalytic reactions in controlled gaseous environments. By combining the developed in situ electrochemical cell with ion SL we established a versatile method to characterize the EEI in solid-state redox systems and reactive electrochemistry at precisely defined conditions. This capability will advance the molecular-level understanding of processes occurring at EEIs that are critical to many energy-related technologies.

in situ electrochemistry | electrode–electrolyte interface | ion soft-landing | ionic liquid membrane | clusters

Understanding the intrinsic properties of electroactive species on electrode surfaces is critical to the rational design of stable and efficient electrode–electrolyte interfaces (EEIs) in numerous technologically important solid-state electrochemical systems (1, 2). Performance degradation and instability of electrochemical systems mostly stems from undesired side reactions occurring at EEIs (3). Agglomeration and decomposition of redox-active species in supercapacitors, evolution of resistive lithium metal dendrites at the solid–electrolyte interphase in batteries, and dissolution and Ostwald ripening of oxygen reduction reaction (ORR) catalysts such as supported Pt clusters and nanoparticles (NPs) in polymer electrolyte membrane fuel cell (PEMFC) electrodes, are just a few examples of common undesirable processes occurring at EEI that require detailed in situ characterization (3). A fundamental understanding of molecular mechanisms and electrode kinetics is key to the future improvement of the performance of EEIs and the longevity and commercial success of electrochemical technologies. The distribution and adsorption/desorption of counterions on electrode surfaces, and subsequent ion exchange and electron transfer are vital processes that define the complexity of operating EEIs that are currently being studied using in situ and *operando* characterization as well as high-level computational modeling (4).

Numerous in situ approaches have been developed for simultaneous electrochemical and physical characterization of EEIs (4, 5). Notable examples include magnetic resonance, infrared spectroscopy, photon- and neutron-based scattering approaches, electron microscopy, and the electrochemical quartz crystal microbalance (4, 5). Although there is substantial interest in understanding processes occurring at porous nanostructured solid-state EEIs, the majority of in situ approaches rely on specially designed liquid electrochemical cells. New approaches for studying solid EEIs, therefore, will benefit numerous applications in catalysis, energy conversion, and storage.

The ability to precisely control the presence of ions of interest at solid-state EEIs is essential to understanding their inherent activity. In this study, we report the development of a unique approach that enables in situ electrochemical characterization of ions on a nanostructured solid-state EEI precisely designed using soft-landing (SL) of mass- and charge-selected ions (6–12). Previously, the superior performance of EEIs prepared using SL in comparison with drop casting and electrospray deposition was demonstrated (13). The high specific capacitance and improved stability of EEIs prepared using SL was attributed to the absence of strongly coordinating counterions and uniform deposition of discrete redox-active ions on the electrode. SL efficiently eliminates unwanted contaminants such as inactive counterions and solvent molecules that are commonly present at EEIs prepared using traditional techniques including direct painting, ambient air spray, and electrodeposition (3). Elimination of strongly coordinating counterions and solvent molecules that alter the distribution and stoichiometry of the compounds of interest at EEI facilitates characterization of the intrinsic activity of precisely defined species.

Significance

In situ characterization of kinetics at electrode–electrolyte interfaces (EEIs) is crucial to the rational design of efficient and sustainable solid-state electrochemical technologies. A significant advancement has been made to rationally understand processes at EEIs using solid-state in situ thin-film electrochemical cells fabricated using specially designed ionic liquid membranes with excellent mass-transfer properties. The in situ cells are used to characterize well-defined EEIs generated using ion soft-landing (SL) in controlled environments, both in vacuum and in the presence of reactant gases. Populating EEIs with precisely defined electroactive species using SL facilitates molecular-level understanding of electron transfer processes within deposited species and between species and electrodes, thus providing a powerful methodology to characterize technologically relevant EEIs during operation.

Author contributions: V.P., G.E.J., and J.L. designed research; V.P. and G.E.J. performed research; V.P., G.E.J., and B.W. contributed new reagents/analytic tools; V.P., G.E.J., and J.L. analyzed data; and V.P., G.E.J., and J.L. wrote the paper.

The authors declare no conflict of interest.

This article is a PNAS Direct Submission.

[1]Present address: State Key Laboratory of Marine and Environmental Science and College of Ocean and Earth Sciences, Xiamen University, Xiamen 361102, China.

[2]To whom correspondence should be addressed. Email: Julia.Laskin@pnnl.gov.

This article contains supporting information online at www.pnas.org/lookup/suppl/doi:10.1073/pnas.1608730113/-/DCSupplemental.

In situ electrochemical characterization of soft-landed size-selected metal clusters has been achieved previously by Anderson and coworkers using an elegantly designed in-vacuum liquid electrochemical cell (14, 15). These pioneering studies demonstrated substantial damage of glassy carbon electrodes containing soft-landed Pt clusters upon exposure to air and water, highlighting the importance of characterizing the EEI in vacuum. An approach introduced here is a demonstration of in situ electrochemical studies of precisely selected electroactive species on a solid EEI in a controlled environment. This is achieved by designing and fabricating a solid-state thin-film electrochemical cell that is stable both under vacuum and under controlled gas conditions (gas permeable). The cell is composed of a solid porous ionic liquid (IL) membrane on a screen-printed electrode (SPE) (Fig. 1). Due to a wide operating potential range, extremely low vapor pressure, and the absence of side reactions caused by solvent molecules, ILs have been used as state-of-the-art high-performance electrolytes in electrochemical systems such as batteries, supercapacitors, fuel cells, and CO_2 conversion catalysts (16–18). For the same reasons, vacuum-based liquid electrochemical cells using ILs have been used for in situ characterization (19). Herein, we introduce solid-state three-electrode electrochemical cells (also known as half-cells) incorporating thin IL membranes for in situ characterization of solid EEIs. Importantly, the in situ electrochemical cell designed using a porous IL membrane mimics the nanostructured electrolyte widely used in many state-of-the-art solid-state electrochemical devices (16).

The in situ cells reported in this study enable (*i*) characterization of both intrinsic redox and reactive processes with control over the stoichiometry and distribution of analyte species at EEIs in nanostructured solid-state electrolyte under well-controlled conditions and (*ii*) understanding of the effect of diffusion of ions of interest through pores on their electrochemical activity. Remarkably, it is demonstrated that the rates of diffusion-limited charge-transfer processes in the solid IL membranes are comparable to those observed in liquid electrolytes. In addition, the diffusion of electroactive species in the porous electrolyte layer is similar to that observed in solid-state energy conversion and storage devices (16, 20), thereby emulating technologically relevant mass-transfer conditions.

In redox electrochemistry, Keggin molybdenum polyoxometalate (POM) anions ($PMo_{12}O_{40}$), stable clusters with multielectron redox activity, are used as a model system. The transfer of up to 24 electrons (e^-) was reported for $PMo_{12}O_{40}$ with retention of its structural integrity making this cluster a promising active material for rechargeable batteries and water electrolyzers (21, 22). SL is used to populate EEIs with different charge states of $PMo_{12}O_{40}$ (3- and 2-) and complementary fragments of $PMo_{12}O_{40}$ generated using in-source collision-induced dissociation (CID) to examine the effect on POM redox activity. Reactive electrochemistry experiments (also referred to as catalytic processes) are performed by examining ORR on soft-landed bare Pt cluster ions ~1 nm in diameter produced by magnetron sputtering and gas aggregation. SL of bare metal clusters onto the cell eliminates the need to use stabilizing ligands or solvent molecules that may affect cluster properties, and thus provides a direct route for studying intrinsic electrocatalytic activity. This study is a demonstration of the combination of in situ thin-film electrochemical cells with SL as a versatile approach to explore both the redox and reactive electrochemical processes of selected species at well-defined EEIs, which accurately represents the half-cell conditions of many technologically important electrochemical systems.

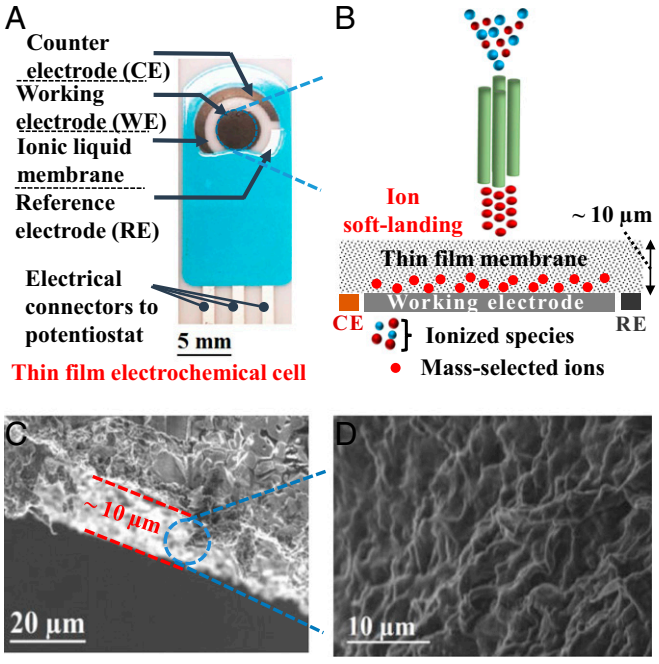

Fig. 1. (*A*) Image of the three-electrode solid-state in situ IL electrochemical cell for performing redox and reactive electrochemistry. (*B*) Schematic representation of a well-defined EEI prepared using SL. (*C* and *D*) Scanning electron micrographs of the cross-section and interior of the IL membrane present in the in situ IL cell, respectively.

Results and Discussion

Characterization of the in Situ Electrochemical Cells. Two types of thin-film electrochemical cells with different IL membranes are developed in this study. Cell 1 is composed of a 1-ethyl-3-methylimidazolium tetrafluoroborate ($EMIMBF_4$)-based aprotic IL membrane with cobaltocene/cobaltocenium (Cc/Cc^+) as an internal reference redox couple (IRRC) on a Pt SPE. Two variants of cell 2 contain (*i*) an IL membrane prepared using aprotic $EMIMBF_4$ IL and protic trifluoroacetic acid-2-methylpyridine IL, and (*ii*) a Nafion membrane prepared (using a 5 wt% solution obtained from Sigma-Aldrich) to mimic a conventional PEMFC interface. Both variants of cell 2 are without an IRRC on an indium-tin-oxide (ITO) SPE. The presence of protons in cell 2 makes a nonpolarizable interface at the Ag reference electrode (RE) that acts as a pseudoreference electrode. The formation of a nearly perfect electric double layer (EDL) and efficient diffusion of ions and reactant gases within the in situ cells are important considerations for their design and performance. A detailed description of the development and optimization of the in situ thin-film electrochemical cells is presented in the *SI Appendix*. Briefly, cyclic voltammetry (CV) of cell 1 indicates (*i*) a wide operating potential range of −1,700–1,000 mV vs. Ag (all potential mentioned hereafter are with reference to Ag) (Fig. 2 and *SI Appendix*, Fig. S1 and S2); (*ii*) stable rectangular non-Faradaic behavior typical of a $1e^-$ redox process of the IRRC (Cc/Cc^+) with the formal potential at ~1,480 mV (Fig. 2 and *SI Appendix*, Fig. S2); (*iii*) efficient diffusion of ions [diffusion coefficient of $(4.9 \pm 2.1) \times 10^{-7}$ cm^2/s for Cc/Cc^+ in $EMIMBF_4$] in the IL membrane as determined by CV of Cc/Cc^+ at different scan rates (*SI Appendix*, Fig. S2 and Table S1) using the Randles–Sevcik equation (*SI Appendix*, Eq. **S1**). The value of the diffusion coefficient is of the same order of magnitude as values reported in the literature ($\sim 1.1 \times 10^{-7}$ cm^2/s) for Cc/Cc^+ in pristine $EMIMBF_4$ (23). It is notable that excellent mass transfer at EEI in solid-state cell 1 is achieved in comparison with liquid electrochemical cells. Furthermore, the diffusion coefficient of $\sim(6.0 \pm 3.2) \times 10^{-7}$ cm^2/s and the Nernst diffusion layer thickness of ~100 nm estimated by analysis of electrochemical impedance spectroscopy (EIS) data obtained with cell 1 (*SI Appendix*, Fig. S3 *A* and *C* and Eqs. **S2–S4**) are comparable to the values obtained from CV, which corroborates the analysis of the EIS data. The Nernst diffusion layer thickness is well below the total thickness of the IL membrane (~10 μm) determined by scanning electron

CHEMISTRY

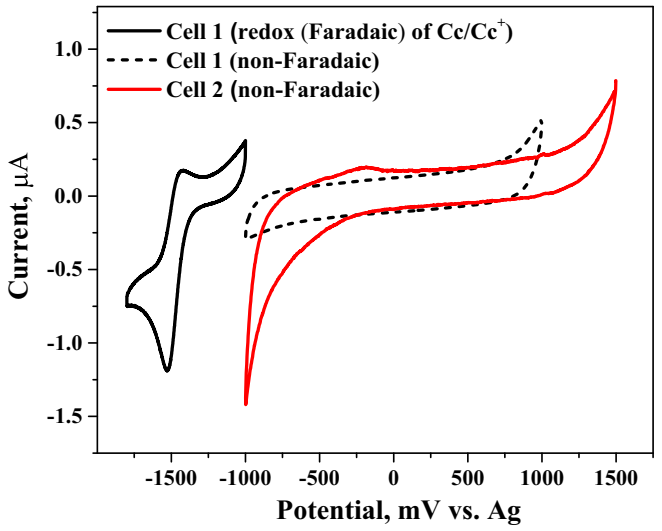

Fig. 2. CVs of the (*i*) aprotic in situ cell (cell 1) acquired in two potential ranges in vacuum to represent the redox (Faradaic) behavior of the Cc/Cc^+ IRRC observed between −1,800 and −1,000 mV vs. Ag, and a typical EDL (non-Faradaic) behavior observed between −1,000 and 1,000 mV vs. Ag; scan rate, 10 mV s^{-1} and (*ii*) protic in situ IL cell (cell 2) acquired in vacuum to present the non-Faradaic behavior observed between −1,000 and 1,500 mV vs. Ag; scan rate, 10 mV s^{-1}.

micrographs (Fig. 1*C*), which ensures a surplus amount of electrolyte ions in the bulk diffusion region. These results indicate that ions deposited on the top surface of the IL membrane readily diffuse to the underlying electrode much like in liquid cells. Similarly, the diffusion coefficient of ions of $(7.9 \pm 1.9) \times 10^{-7}$ cm^2/s and the Nernst diffusion layer thickness of ~2.6 μm are calculated using the EIS data for cell 2 with IL in vacuum (*SI Appendix*, Fig. S3 *B*, *2* and Eqs. **S2–S4**). The diffusion coefficient is of the same order of magnitude as the value determined for typical proton-conducting membranes used in PEMFCs (e.g., $\sim 5 \times 10^{-7}$ cm^2/s for Nafion) (24). An increase in diffusion layer thickness is attributed to increased ionic diffusion due to higher occupancy of smaller H^+ ions at the electrode surface and the smaller surface area of the ITO compared with Pt working electrode (WE). For cell 2 with Nafion, the diffusion coefficient and Nernst diffusion layer thickness are estimated to be 2.5×10^{-8} cm^2/s and 24 nm, respectively (*SI Appendix*, Fig. S3 *B*, *2*). The diffusion coefficient of the Nafion is smaller than the literature values, which is attributed to the lower thickness of Nafion used in this study.

In Situ Redox Electrochemistry of POM Anions. Redox properties of both intact POM anions present in solution ($PMo_{12}O_{40}^{3-}$ and $HPMo_{12}O_{40}^{2-}$) and POM fragments ($Mo_7O_{22}^{2-}$ and $PMo_5O_{18}^{-}$) generated by gas-phase CID that cannot be produced in solution are soft-landed at a kinetic energy of 30 eV per charge (*SI Appendix*, Figs. S4–S6) and examined using cell 1. CV of the soft-landed anions is performed in vacuum after deposition of $\sim 1 \times 10^{14}$ ions on cell 1. Typical CVs of $PMo_{12}O_{40}^{3-}$ and $HPMo_{12}O_{40}^{2-}$ anions at a scan rate of 10 mV s^{-1} are shown in Fig. 3*A*. CVs acquired at different scan rates are shown in *SI Appendix*, Figs. S7 and S8. The CV curves were shifted manually during data processing to maintain the reduction potential of Cc/Cc^+ at the value of −1,520 mV observed before SL. The CVs acquired at different scan rates demonstrate that all of the peaks follow typical Randles–Sevcik behavior. The estimated electrochemical parameters including oxidation and reduction peak potentials ($E_{p,ox}$ and $E_{p,red}$), current functions (R_{ox} and R_{red}) (current function is the ratio of the peak current to the square root of the scan rate), and the number of electrons transferred (n) for the first five and for all redox peaks of $PMo_{12}O_{40}^{3-}$ and $HPMo_{12}O_{40}^{2-}$ are summarized in Table 1 and *SI Appendix*, Table S2, respectively.

Eight reversible redox couples in which the third and sixth peaks correspond to $2e^-$ while the other peaks correspond to $1e^-$ transfer processes are present in the CV of $PMo_{12}O_{40}^{3-}$. In contrast, only five redox peaks are observed for $HPMo_{12}O_{40}^{2-}$ with the third and fifth peaks corresponding to $2e^-$ transfer processes. The peak potentials of the two charge states of POM are in agreement with values reported previously for $[PMo_{12}O_{40}]$ (25), which validates the accuracy of cell 1. The formal redox potentials (E_f) of peaks 1–5 of $PMo_{12}O_{40}^{3-}$ and $HPMo_{12}O_{40}^{2-}$ calculated by the average of $E_{p,ox}$ and $E_{p,red}$ indicate no changes associated with the energy barriers for each redox step as a function of the POM charge state. The number of electrons transferred in the first four redox steps is similar for both $PMo_{12}O_{40}^{3-}$ and $HPMo_{12}O_{40}^{2-}$. A clear deviation in the mechanism of electron transfer processes for the two charge states is observed starting only from the fifth redox peak. The $[PMo_{12}O_{40}]$ anions undergo $2e^-/2H^+$ transfer in protic and $1e^-$ transfer in aprotic electrolytes (25). The presence of trace amounts of protons resulting from deprotonation of $HPMo_{12}O_{40}^{2-}$ in the electrolyte or on the electrode surface may be responsible for the earlier onset of the $2e^-$ processes observed for the 2− charge state of POM. Furthermore, distinct differences are observed in the current functions (R_{ox} and R_{red}) listed in Table 1. Higher values of R_{ox} in comparison with R_{red} are attributed to differences in the oxidation and reduction parts of the EDL formed by asymmetric electrolyte ions ($EMIM^+$ and BF_4^-) (26). The R_{ox} of the first two redox peaks (1, 2) are similar for both charge states. However, a significant decrease in R_{ox} is observed for $HPMo_{12}O_{40}^{2-}$ in comparison with $PMo_{12}O_{40}^{3-}$ for peaks 3–5. The decrease is attributed to the presence of H^+ ions in $HPMo_{12}O_{40}^{2-}$ that may inhibit electron transfer to POM. These results demonstrate the exceptional

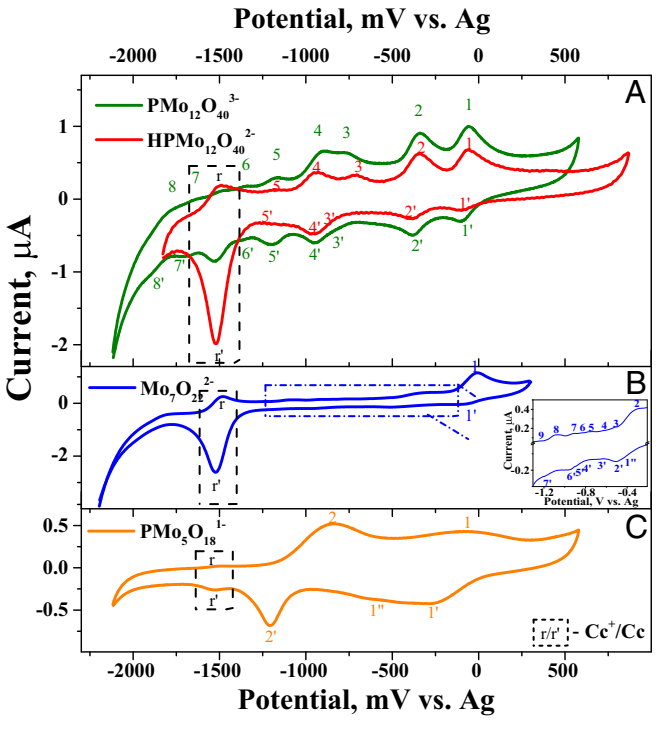

Fig. 3. CVs of cell 1 with soft-landed (*A*) $PMo_{12}O_{40}^{3-}$ and $HPMo_{12}O_{40}^{2-}$ anions, and major fragments of $PMo_{12}O_{40}^{3-}$, (*B*) $Mo_7O_{22}^{2-}$, and (*C*) $PMo_5O_{18}^{-}$. (*B*, *Inset*) Enlarged region between −1,300 and −200 mV. All CVs were performed at a scan rate of 10 mV s^{-1}. Approximately 1×10^{14} ions were deposited in each case. Dashed black rectangles highlight oxidation (r′) and reduction (r) peaks of the Cc/Cc^+ IRRC.

Table 1. Estimated electrochemical parameters including oxidation ($E_{p,ox}$) and reduction ($E_{p,red}$) peak potentials, oxidation (R_{ox}) and reduction (R_{red}) current functions, and the number of electrons (n) transferred for the first five peaks observed for $PMo_{12}O_{40}^{3-}$, $HMo_{12}O_{40}^{2-}$, $Mo_7O_{22}^{2-}$, and $PMo_5O_{18}^{-}$ measured using cell 1

	$PMo_{12}O_{40}^{3-}$			$HPMo_{12}O_{40}^{2-}$			$Mo_7O_{22}^{2-}$				$PMo_5O_{18}^{-}$			
	$E_{p,ox}/E_{p,red}$,	R_{ox}/R_{red},		$E_{p,ox}/E_{p,red}$,	R_{ox}/R_{red},		$E_{p,ox}$,	$E_{p,red}$,	R_{ox},	R_{red},	$E_{p,ox}$,	$E_{p,red}$,	R_{ox},	R_{red},
Peak no.	mV	$A/(V/s)^{-0.5}$	n	mV	$A/(V/s)^{-0.5}$	n	mV		$A/(V/s)^{-0.5}$		mV		$A/(V/s)^{-0.5}$	
1	−64/−90	234/120	1	−67/−90	244/67	1	0	−61	404	89	−46	−233	66	164
2	−350/−380	226/152	1	−353/−385	239/88	1	−351	−419	45	8	−877	−450	175	16
3	−765/−810	152/40	2	−717/−740	82/43	2	−529	−507	5	25	—	−659	—	7
4	−921/−950	203/132	1	−960/−950	139/132	1	−641	−670	2	2	—	−860	—	288
5	−1,170/−1,173	51/71	1	−1,184/−1,165	14/28	2	−777	−790	4	4	—	−1,197	—	21

Current function, $R_{ox} = (i_{p,ox}/\sqrt{\nu})/10^{-8}$ and $R_{red} = (i_{p,red}/\sqrt{\nu})/10^{-8}$, where $i_{p,ox}$ and $i_{p,red}$ are oxidation and reduction peak currents, respectively (A), ν –scan rate (V/s).

capability of cell 1 combined with ion SL to explore the charge-state dependence of the redox pathways of complex ions at EEIs, something that is not possible with other techniques.

Redox properties of complementary building blocks of $[PMo_{12}O_{40}]$ that contribute to the overall multielectron redox activity of the intact cluster are also examined in this study. The electronic properties of $[PMo_{12}O_{40}]$ in the gas phase have been extensively studied (27, 28), but intramolecular charge transfer which is critical for efficient participation of all Mo atoms of the $[PMo_{12}O_{40}]$ cluster in multielectron redox processes at EEIs has not been explored. CID combined with SL is ideally suited for studying the structures and reactivity of ionic species that cannot be prepared in solution (29, 30). Previously, a substantial difference was observed in the chemical reactivity of SL ruthenium trisbipyridine dications, $Ru(bpy)_3^{2+}$, [bpy = Tris(bipyridine) ligand] and their undercoordinated analog, $Ru(bpy)_2^{2+}$, produced using in-source CID (29). Similar observations were also made for fully and partially phosphine-ligated gold cluster cations generated by CID (30). In this study, mass-selected $Mo_7O_{22}^{2-}$ and $PMo_5O_{18}^{-}$ fragments, generated by CID, are deposited onto different in situ cells (cell 1) and their redox activity is characterized using CV.

The CVs of both $Mo_7O_{22}^{2-}$ (Fig. 3*B*) and $PMo_5O_{18}^{-}$ (Fig. 3*C*) show a combination of reversible and irreversible oxidation and reduction peaks. The CV of $Mo_7O_{22}^{2-}$ shows 10 oxidation peaks and 8 reduction peaks, whereas the CV of $PMo_5O_{18}^{-}$ contains 2 oxidation peaks and 5 reduction peaks. All of the peaks follow Randles–Sevcik behavior (*SI Appendix*, Figs. S9 and S10). The number of redox peaks observed for $Mo_7O_{22}^{2-}$ matches the number of peaks observed for $PMo_{12}O_{40}^{3-}$ within the same potential range (Fig. 3 *A* and *B*). Similar peak potentials are observed for the first three reversible peaks of $PMo_{12}O_{40}^{3-}$ and $Mo_7O_{22}^{2-}$ (Table 1). The first oxidation and reduction peaks (peak 1) of $PMo_{12}O_{40}^{3-}$ are shifted by 60 and 30 mV, respectively, toward lower values in comparison with $Mo_7O_{22}^{2-}$, and the calculated R_{ox} of the first peak is substantially lower than the value obtained for $Mo_7O_{22}^{2-}$. These findings indicate that electron transfer in the first redox couple is more efficient for $Mo_7O_{22}^{2-}$ compared with $PMo_{12}O_{40}^{3-}$. In contrast, substantially lower R_{ox} and R_{red} values are observed for all other redox peaks of $Mo_7O_{22}^{2-}$ in comparison with $PMo_{12}O_{40}^{3-}$ (Table 1 and *SI Appendix*, Table S3). This observation indicates inefficient electron transfer from the $Mo_7O_{22}^{2-}$ cluster to the electrode in all subsequent redox steps.

In contrast, the CV of the $PMo_5O_{18}^{-}$ fragment is characterized by broad oxidation and reduction peaks with significantly higher values of R_{ox} and R_{red} over the entire potential range (Fig. 3*C* and Table 1).The difference in the width and intensity of the oxidation and reduction peaks of $Mo_7O_{22}^{2-}$ and $PMo_5O_{18}^{-}$ may be attributed either to changes in adsorption of these ions on the electrode surface due to variations in their effective dipole moments or the presence of overlapping peaks corresponding to multiple isomers with distinct electronic properties as described in previous computational studies (31). The presence of narrow redox peaks in the CVs for both fragments rules out the possibility of dissimilar adsorption on the WE, which would influence each of the peaks systematically. Therefore, it is most likely that the broad first reduction and oxidation peaks observed for $PMo_5O_{18}^{-}$ originate from the presence of multiple isomers with substantially different overpotentials that contribute to several overlapping redox peaks in the CV. Furthermore, except for peak 1 of $Mo_7O_{22}^{2-}$, substantially higher values of R_{ox} and R_{red} are observed for all the rest of the peaks for $PMo_5O_{18}^{-}$ in comparison with $Mo_7O_{22}^{2-}$ (Table 1). In the case of Keggin $PMo_{12}O_{40}^{3-}$, where these two fragments are assembled together, higher R_{ox} and R_{red} values are observed for all redox peaks.

The CV results may be rationalized by assuming that redox properties of $PMo_{12}O_{40}^{3-}$ are affected by the synergistic interaction between the two building blocks, $Mo_7O_{22}^{2-}$ and $PMo_5O_{18}^{-}$, and electron transfer within the cluster. These observations provide information about the contribution of individual building blocks of metal oxide clusters to the overall redox activity. To confirm that the POM anions are deposited intact on the cell surface, identical SL experiments were conducted at a lower kinetic energy of 5 eV per charge. Similar CVs were obtained for the soft-landed POM anions at the two different kinetic energies (*SI Appendix*, Fig. S11), indicating that POM anions do not undergo dissociation upon landing on the cell surface. Collectively, these results demonstrate that SL combined with the in situ cell developed in this study constitutes a powerful tool for characterizing the intrinsic redox properties of complex redox-active species at well-defined EEIs, including species that cannot be prepared in solution.

Reactive Electrochemistry on Bare Pt Clusters. The ORR activity (catalytic process) on well-defined soft-landed bare Pt clusters ($\sim Pt_{30}$) is evaluated using protic IL to demonstrate the ability of the thin-film electrochemical cell to mimic the acidic electrolyte environment relevant to traditional catalytic studies in aqueous solution. A comparative ORR experiment was also performed using cell 2 with Nafion. Of note is that ORR on Pt follows a four-electron pathway in both protic IL and aqueous acidic electrolyte (e.g., Nafion) (32) and the intrinsic ORR activity should not change between protic IL and Nafion electrolyte. Approximately 2×10^{12} bare anionic Pt clusters produced by magnetron sputtering and gas aggregation (33, 34) are uniformly deposited onto both variants of cell 2 and characterized by CV under a N_2 or O_2 atmosphere (Fig. 4). The CVs of pristine cell 2 with IL (Fig. 4) and Nafion (*SI Appendix*, Fig. S12*A*) under N_2 show characteristic non-Faradaic behavior in the potential range where ORR is known to occur, which confirms the stability of the cell. In comparison, in an O_2 atmosphere, pristine cell 2 with IL reveals the presence of the ORR at an onset potential of −750 mV and the ORR current measured at −1,000 mV was −3.7 μA. No

CHEMISTRY

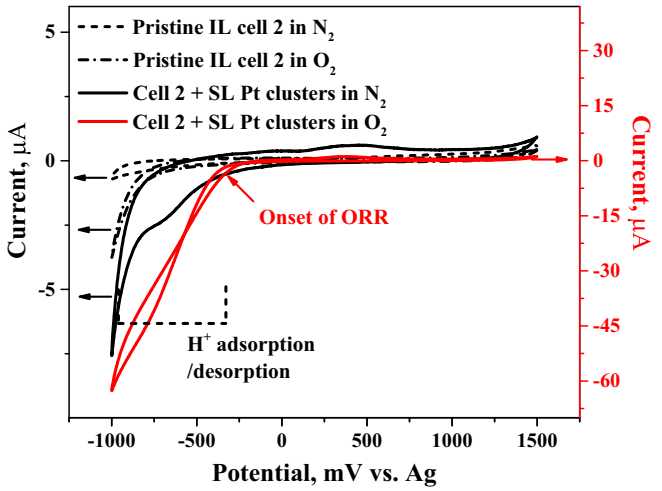

Fig. 4. CVs of pristine cell 2 with IL, and IL cell 2 containing 2×10^{12} soft-landed bare Pt clusters acquired under N_2 and O_2 atmosphere. ORR activity is observed for both pristine cell and cell containing soft-landed Pt clusters in O_2. Scan rate, 50 mV s^{-1}.

significant ORR current was observed in pristine cell 2 with Nafion in the presence of O_2. In contrast, the CV of cell 2 with IL membrane containing soft-landed Pt clusters acquired in a N_2 atmosphere shows the characteristic H^+ adsorption and desorption regions arising from the presence of protons in the fully dehydrated proton-conducting IL membrane. The H^+ adsorption and desorption regions do not exhibit well-defined peaks corresponding to specific Pt facets because small (~1 nm) Pt clusters do not contain such well-defined facets like larger NPs (35). The calculated electrochemically active surface area (ECSA) of 38 m^2/g_{Pt} using *SI Appendix*, Eq. **S5** is comparable to values reported previously for Pt-based catalysts (36), indicating that most of the deposited Pt clusters reach the electrode surface after SL. Cell 2 with Nafion in the presence of bare Pt clusters and humidified N_2 shows significant reduction current below 0 V, which is attributed either to H^+ adsorption and desorption or H_2 evolution. Due to this uncertainty, the ECSA was not estimated in this case. For cell 2 with IL, Pt clusters in an O_2 atmosphere show well-resolved ORR curves characterized by an increase of 60 μA reduction current at −1,000 mV with an onset potential of −300 mV, which is 450 mV higher than the onset of ORR on pristine cell 2 without clusters. The area-specific and mass-specific activity was estimated to be 677 $\mu A/cm^2$ and 0.26 A/mg_{Pt}, respectively. The decrease of 100 mV in the onset potential and higher specific activities observed for Pt clusters in comparison with literature values (37) is attributed to the superior ORR activity of the soft-landed species. It follows that the proton-conducting IL membrane used in this study facilitates diffusion of O_2 to the electrode surface and provides sufficient amounts of protons to promote the ORR. For comparison, significant ORR activity was observed for cell 2 with Nafion on bare Pt clusters with the onset potential of 500 mV and reduction current of 23 μA (*SI Appendix*, Fig. S12*B*). A significant Pt oxide formation at ~510 mV was observed typical of the ORR occurring in aqueous acidic electrolyte. The observed onset potential of the ORR is lower than the values reported for ORR in Nafion, indicating the lower ORR activity of Pt clusters in this cell (36). This could be attributed to either an increase in interfacial resistance due to immobilization or agglomeration of bare Pt clusters on the electrode interface, both of which may result in an increase in the overpotential. The ability to study reactive electrochemistry using cell 2 opens up opportunities for examining the catalytic activity of well-defined bare clusters and NPs that cannot be generated using traditional synthesis approaches.

In summary, the in situ thin-film electrochemical cells reported in this study are ideally suited for characterizing redox and reactive processes at well-defined EEIs. The thin-film cells are compatible with various state-of-the-art deposition techniques and demonstrate excellent stability in diverse controlled environments ranging from high vacuum to atmospheric pressure. Furthermore, cells 1 and 2 exhibit comparable mass-transfer properties at the EEI as evidenced by their estimated diffusion coefficients, in comparison with liquid electrochemical cells and commercial PEMFC electrolytes, respectively. These results indicate that much like in liquid electrochemical cells, ions deposited onto the surface of the solid IL membranes readily diffuse to the WE to participate in redox processes. Several examples presented in this study demonstrate the potential of the in situ cells combined with SL and in-source CID for studying redox properties of novel states of both intact ions and their fragments. This provides detailed insights into the contribution of different building blocks to the overall redox activity of clusters that cannot be studied experimentally using existing approaches. In addition, in situ proton-conducting IL cells may be used for examining the electrocatalytic activity of bare metal clusters formed in the gas phase that are not accessible using synthesis in solution. The approach offers a platform to study critical electrochemical processes taking place in functional devices and thus acquire an in-depth understanding of electrode kinetics which may lead to rational design of efficient, sustainable, and high-performance EEI for solid-state electrochemical systems with applications in catalysis as well as energy conversion and storage.

Materials and Methods

Fabrication of in Situ IL Thin-Film Electrochemical Cells. Two types of in situ IL cells were fabricated on commercially available Pt and ITO SPE electrodes (Dropsens, Spain) for studying redox and reactive electrochemistry, respectively. Cell 1 containing a nonaqueous aprotic IL membrane on Pt SPE was used for studying the intrinsic redox activity of soft-landed ions, whereas cells containing a nonaqueous proton-conducting IL membrane (cell 2) on ITO SPE were used for examining the electrocatalytic activity of bare Pt clusters toward the ORR. Another variant of cell 2 was prepared with a thin Nafion membrane instead of IL membrane to represent the conventional PEMFC interface. The Pt SPE consists of a Pt working electrode (WE), Pt counterelectrode (CE), and Ag reference electrode (RE) as shown in Fig. 1*A*. The ITO SPE consists of an ITO-coated WE, carbon CE, and Ag RE. The approximate geometric area of the WE for both Pt and ITO SPEs is 7×10^{-6} m^2. Further details describing the preparation of in situ cells are provided in the *SI Appendix*. The cell holder is equipped with a three-pin connector wired to an electrical vacuum feedthrough providing electrical connections from the WE, CE, and RE to a potentiostat (Versastat 3, Princeton Applied Research).

Morphology of the IL Membrane of the in Situ Cell. The surface morphology and thickness of the IL membrane of cell 1 was examined using an scanning electron microscopy (SEM) (Quanta 3D model, FEI, Inc.) operated at 10-kV acceleration voltage. The fabricated in situ cell was cut with a razor blade and the cross-section of the IL membrane on top of the WE was examined. Similarly, the layer of IL membrane was peeled off to examine its interior.

SL of Redox-Active Cluster Ions and Bare Pt Cluster Ions. Two SL instruments described in more detail in the *SI Appendix* were used in this study. In the first instrument, shown in *SI Appendix*, Fig. S4 (38, 39), ions are produced using electrospray ionization (ESI) of $Na_3[PMo_{12}O_{40}]$ xH_2O in methanol and transferred into the vacuum system using a heated stainless steel inlet where they undergo desolvation. Ions are subsequently transferred using a dual ion funnel system, mass-selected using a quadrupole mass filter, and deposited onto the electrochemical cell at a kinetic energy of 30–35 eV per charge. Additional experiments were performed with lower kinetic energy of 5 eV per charge to confirm that POM anions are deposited intact on the cell surface. The total number of ions deposited was calculated by integrating the ion current over time. A typical ESI mass spectrum of a $Na_3[PMo_{12}O_{40}]$ solution (*SI Appendix*, Fig. S5) contains stable $PMo_{12}O_{40}^{3-}$ and $HPMo_{12}O_{40}^{2-}$ anions at m/z = 608 and 911, respectively (40, 41), both of which were examined in this study. In addition, the two most abundant complementary fragment ions, $Mo_7O_{22}^{2-}$ (m/z = 512) and $PMo_5O_{18}^{-}$ (m/z = 798), produced by in-source CID of $PMo_{12}O_{40}^{3-}$ (*SI Appendix*, Fig. S6) (40) were mass-selected and deposited onto the in situ IL cell. In CID, molecular ions are accelerated by electric fields and fragment ions are generated through energetic collisions

of precursor ions with neutral gas molecules. In this study, in-source CID was achieved by increasing the rf of both ion funnels and adjusting the potential difference between the end plate of the second ion funnel and the dc offset of the collisional quadrupole. In the second instrument, SL of bare anionic Pt clusters was achieved using the modified commercial Nanogen-Trio cluster source and Q-Prep 500 deposition system (Mantis Deposition Ltd.) (33, 34). The bare anionic Pt clusters were produced by dc magnetron sputtering of a circular Pt target in a controlled flow of ultra high-purity argon and helium and deposited onto cell 2 without mass selection. The peak of the anionic Pt cluster distribution was maintained at ~6,000 amu corresponding to ~Pt_{30} and a cluster size of ~1 nm.

Electrochemical Experiments. CV and EIS were used to study the characteristics of the in situ IL cells (cells 1 and 2). CV was used to determine the redox electrochemistry of SL POM anions using cell 1 and ORR activity (reactive electrochemistry) of bare Pt clusters using two variants of cell 2, respectively. Further details describing the electrochemical experiments performed using cells 1 and 2 are provided in the *SI Appendix*. All CV and EIS experiments presented in this study were repeated at least five times.

ACKNOWLEDGMENTS. This work was supported by the US Department of Energy (DOE), Office of Science, Office of Basic Energy Sciences, Chemical Sciences, Geosciences and Biosciences Division. The research was performed using Environmental Molecular Sciences Laboratory, a national scientific user facility sponsored by the DOE's Office of Biological and Environmental Research and located at Pacific Northwest National Laboratory (PNNL). PNNL is operated by Battelle for DOE under Contract DE-AC05-76RL01830.

1. Bard AJ, et al. (1993) The electrode/electrolyte interface - a status report. *J Phys Chem* 97(28):7147–7173.
2. Srinivasan S (2006) Electrode/electrolyte interfaces: Structure and kinetics of charge transfer. *Fuel Cells: From Fundamentals to Applications*, ed Srinivasan S (Springer US, Boston), pp 27–92.
3. Shen PK, Wang C-Y, Jiang SP, Sun X, Zhang J (2015) *Electrochemical Energy: Advanced Materials and Technologies* (CRC Press, Boca Raton, FL), pp 1–170.
4. Forse AC, Merlet C, Griffin JM, Grey CP (2016) New perspectives on the charging mechanisms of supercapacitors. *J Am Chem Soc* 138(18):5731–5744.
5. Itkis DM, et al. (2015) Probing operating electrochemical interfaces by photons and neutrons. *ChemElectroChem* 2(10):1427–1445.
6. Grill V, Shen J, Evans C, Cooks RG (2001) Collisions of ions with surfaces at chemically relevant energies: Instrumentation and phenomena. *Rev Sci Instrum* 72(8):3149–3179.
7. Johnson GE, Hu Q, Laskin J (2011) Soft landing of complex molecules on surfaces. *Annu Rev Anal Chem* 4:83–104.
8. Cyriac J, Pradeep T, Kang H, Souda R, Cooks RG (2012) Low-energy ionic collisions at molecular solids. *Chem Rev* 112(10):5356–5411.
9. Verbeck G, Hoffmann W, Walton B (2012) Soft-landing preparative mass spectrometry. *Analyst (Lond)* 137(19):4393–4407.
10. Johnson GE, Gunaratne D, Laskin J (2016) Soft- and reactive landing of ions onto surfaces: Concepts and applications. *Mass Spectrom Rev* 35(3):439–479.
11. Rauschenbach S, et al. (2006) Electrospray ion beam deposition of clusters and biomolecules. *Small* 2(4):540–547.
12. Laskin J, Johnson GE, Prabhakaran V (2016) Soft-landing of complex ions for studies in catalysis and energy storage. *J Phys Chem C* 120:23305–23322.
13. Prabhakaran V, et al. (2016) Rational design of efficient electrode-electrolyte interfaces for solid-state energy storage using ion soft landing. *Nat Commun* 7:11399.
14. von Weber A, Baxter ET, White HS, Anderson SL (2015) Cluster size controls branching between water and hydrogen peroxide production in electrochemical oxygen reduction at Ptn/ITO. *J Phys Chem C* 119(20):11160–11170.
15. Proch S, Wirth M, White HS, Anderson SL (2013) Strong effects of cluster size and air exposure on oxygen reduction and carbon oxidation electrocatalysis by size-selected Pt(n) ($n \leq 11$) on glassy carbon electrodes. *J Am Chem Soc* 135(8):3073–3086.
16. MacFarlane DR, et al. (2016) Ionic liquids and their solid-state analogues as materials for energy generation and storage. *Nat Rev Mat* 1:15005.
17. Huang JY, et al. (2010) In situ observation of the electrochemical lithiation of a single SnO_2 nanowire electrode. *Science* 330(6010):1515–1520.
18. Zhang J, Xia Z, Dai L (2015) Carbon-based electrocatalysts for advanced energy conversion and storage. *Sci Adv* 1(7):e1500564.
19. Wibowo R, Aldous L, Jacobs RMJ, Manan NSA, Compton RG (2011) Monitoring potassium metal electrodeposition from an ionic liquid using in situ electrochemical-X-ray photoelectron spectroscopy. *Chem Phys Lett* 509(1–3):72–76.
20. Tu Z, Nath P, Lu Y, Tikekar MD, Archer LA (2015) Nanostructured electrolytes for stable lithium electrodeposition in secondary batteries. *Acc Chem Res* 48(11):2947–2956.
21. Wang H, et al. (2012) In operando X-ray absorption fine structure studies of polyoxometalate molecular cluster batteries: Polyoxometalates as electron sponges. *J Am Chem Soc* 134(10):4918–4924.
22. Symes MD, Cronin L (2013) Decoupling hydrogen and oxygen evolution during electrolytic water splitting using an electron-coupled-proton buffer. *Nat Chem* 5(5):403–409.
23. Rogers EI, et al. (2008) Voltammetric characterization of the ferrocene|ferrocenium and cobaltocenium|cobaltocene redox couples in RTILs. *J Phys Chem C* 112(7):2729–2735.
24. Sel O, et al. (2013) Determination of the diffusion coefficient of protons in Nafion thin films by ac-electrogravimetry. *Langmuir* 29(45):13655–13660.
25. Sadakane M, Steckhan E (1998) Electrochemical properties of polyoxometalates as electrocatalysts. *Chem Rev* 98(1):219–238.
26. Lockett V, Horne M, Sedev R, Rodopoulos T, Ralston J (2010) Differential capacitance of the double layer at the electrode/ionic liquids interface. *Phys Chem Chem Phys* 12(39):12499–12512.
27. Taketa H, Katsuki S, Eguchi K, Seiyama T, Yamazoe N (1986) Electronic structure and redox mechanism of dodecamolybdophosphate. *J Phys Chem* 90(13):2959–2962.
28. López X, Carbó JJ, Bo C, Poblet JM (2012) Structure, properties and reactivity of polyoxometalates: A theoretical perspective. *Chem Soc Rev* 41(22):7537–7571.
29. Johnson GE, Laskin J (2010) Preparation of surface organometallic catalysts by gas-phase ligand stripping and reactive landing of mass-selected ions. *Chem Eur J* 16(48):14433–14438.
30. Johnson GE, Laskin J (2015) Soft landing of mass-selected gold clusters: Influence of ion and ligand on charge retention and reactivity. *Int J Mass Spectrom* 377:205–213.
31. Li S, Dixon DA (2006) Molecular and electronic structures, Brönsted basicities, and Lewis acidities of group VIB transition metal oxide clusters. *J Phys Chem A* 110(19):6231–6244.
32. Switzer EE, et al. (2013) Oxygen reduction reaction in ionic liquids: The addition of protic species. *J Phys Chem C* 117(17):8683–8690.
33. Johnson GE, Colby R, Engelhard M, Moon D, Laskin J (2015) Soft landing of bare PtRu nanoparticles for electrochemical reduction of oxygen. *Nanoscale* 7(29):12379–12391.
34. Johnson GE, Colby R, Laskin J (2015) Soft landing of bare nanoparticles with controlled size, composition, and morphology. *Nanoscale* 7(8):3491–3503.
35. Markovic NM, Gasteiger HA, Ross PN (1995) Oxygen reduction on platinum low-index single-crystal surfaces in sulfuric acid solution: Rotating ring-Pt(hkl) disk studies. *J Phys Chem* 99(11):3411–3415.
36. Gasteiger HA, Kocha SS, Sompalli B, Wagner FT (2005) Activity benchmarks and requirements for Pt, Pt-alloy, and non-Pt oxygen reduction catalysts for PEMFCs. *Appl Catal B* 56(1–2):9–35.
37. Khan A, Lu X, Aldous L, Zhao C (2013) Oxygen reduction reaction in room temperature protic ionic liquids. *J Phys Chem C* 117(36):18334–18342.
38. Gunaratne KDD, et al. (2015) Design and performance of a high-flux electrospray ionization source for ion soft landing. *Analyst (Lond)* 140(9):2957–2963.
39. Johnson GE, Hadjar O, Laskin J (2011) Characterization of the ion beam focusing in a mass spectrometer using an IonCCD™ detector. *J Am Soc Mass Spectrom* 22(8):1388–1394.
40. Gunaratne KD, Prabhakaran V, Johnson GE, Laskin J (2015) Gas-phase fragmentation pathways of mixed addenda Keggin anions: PMo12-nW nO 40 3- (n = 0-12). *J Am Soc Mass Spectrom* 26(6):1027–1035.
41. Gunaratne KDD, et al. (2014) Controlling the charge state and redox properties of supported polyoxometalates via soft landing of mass-selected ions. *J Phys Chem C* 118(48):27611–27622.

Supplementary Information (SI)

In situ solid-state electrochemistry of mass selected ions at well-defined electrode-electrolyte interfaces

Authors: Venkateshkumar Prabhakaran[1], Grant E. Johnson[1], Bingbing Wang[2,†] and Julia Laskin[1,*]

Author address: [1]Physical Sciences Division, Pacific Northwest National Laboratory, P.O. Box 999, MSIN K8-88, Richland, WA 99352, USA.

[2]Environmental Molecular Sciences Laboratory, Pacific Northwest National Laboratory, Richland, WA 99352, USA.

[†] Present address: State Key Laboratory of Marine and Environmental Science and College of Ocean and Earth Sciences, Xiamen University, Xiamen 361102, China.

[*]Author for correspondence: Julia.Laskin@pnnl.gov

SI text

I. Chemicals. 1-Ethyl-3-methylimidazolium tetrafluoroborate ($EMIMBF_4$) (99%), trifluoroacetic acid (TFA) (99%), 2-methylpyridine (2MP) (98%), poly(vinylidene fluoride-co-hexafluoropropylene) (PVDF-HFP) (ACS grade), anhydrous N,N-dimethylformamide (DMF) (99.8%), sodium phosphomolybdate hydrate ($Na_3[PMo_{12}O_{40}]xH_2O$ (98%), cobaltocenium hexafluorophosphate ($CcPF_6$) (98%), and Nafion® solution (5%) were all purchased from Sigma-Aldrich and used as received.

II. Fabrication of in situ thin film electrochemical cells.

Two types of in situ thin film electrochemical cells were employed in this study. Cell 1 containing a non-aqueous aprotic IL membrane on Pt screen printed electrode (SPE) was used for studying the intrinsic redox activity of SL ions while cell 2 containing a non-aqueous proton-conducting IL membrane on ITO SPE was employed for examining the electrocatalytic activity of bare Pt clusters toward the ORR. Another variant of cell 2 was prepared with a thin Nafion® instead of IL membrane to represent the interface used in conventional polymer electrolyte membrane fuel cells (PEMFCs). Cells 1 and 2 were fabricated on commercially available Pt and ITO SPE electrodes (Dropsens SL, Asturias, Spain) for studying redox and reactive electrochemistry, respectively. The Pt SPE consists of a Pt working electrode (WE), Pt counter electrode (CE), and Ag reference electrode (RE) as shown in Fig. 1(a). The ITO SPE consists of an ITO coated WE, carbon CE, and Ag RE. The approximate geometric area of the WE for both Pt and ITO SPEs is 7×10^{-6} m^2.

Prior to use, the working region of the SPE containing the WE, CE, and RE was washed with anhydrous DMF and dried using N_2 gas. Next, an IL membrane was prepared by mixing IL with a polymer binder and casting 10 µL of the resulting solution onto the working region of the SPE using a 10 µL pipette (Eppendorf Research, Hauppauge, NY). After the solution spread over the entire working region, ~5 µL of the cast solution was pipetted off the surface. During this step, care was taken to avoid contact between the pipette tip and the SPE, as it could damage the WE. These sequential steps of casting and pipetting off the solution ensure that the solution is spread uniformly over the working region of the SPE and forms a thin ionically conducting

membrane covering all three electrodes. The SPE with the IL membrane was subsequently dried under vacuum for one hour and mounted on a custom-designed sample holder for introduction into an ion deposition instrument. The holder is equipped with a three-pin connector wired to an electrical vacuum feedthrough providing electrical connections from the WE, CE, and RE to a potentiostat (Versastat 3, Princeton Applied Research, Oak Ridge, TN).

The aprotic IL membrane containing $EMIMBF_4$ IL and poly(vinylidene fluoride-co-hexafluoropropylene) (PVDF-HFP) copolymer in cell 1 was prepared as follows: 1.5 g of PVDF-HFP was dissolved in 12 mL of DMF and stirred overnight at room temperature to make a homogenous solution. 1.8 mL of $EMIMBF_4$ and 200 µL of 500 µM $CcPF_6$ was added to 12 mL of PVDF-HFP/DMF solution and stirred continuously for 4 hours. $CcPF_6$ is used as an IRRC (Cc/Cc^+) for accurate representation of the WE potential. The pristine $EMIMBF_4$ solution was kept under vacuum at 50ºC for 24 hours to remove traces of water from the IL prior to use.

The proton-conducting IL membrane contains both aprotic $EMIMBF_4$ and protic IL TFA-2MP that help reduce the vapor pressure and introduce protons, respectively. The proton-conducting IL membrane in cell 2 was prepared as follows: 10 mL of TFA was added dropwise to 5 mL of 2MP. The TFA-2MP protic IL was then heated at 60ºC for 48 hours to remove trace amounts of water. Approximately 1 mL of as-prepared TFA-2MP solution was added to 12 mL of PVDF-HFP/DMF solution to prepare a casting solution. This was achieved by first preparing a $EMIMBF_4$/PVDF-HFP solution by mixing 1.5 g of PVDF-HFP dissolved in 12 mL of DMF and 1.8 mL of $EMIMBF_4$, followed by stirring overnight at room temperature. Protic IL was introduced by adding 500 µL of TFA-2MP to 1 ml of $EMIMBF_4$/PVDF-HFP solution. The resultant solution was thoroughly mixed and used to fabricate a proton conducting IL membrane on ITO SPE as described earlier. The abundant presence of protons in the IL membrane makes a non-polarizable interface at the Ag RE that acts as a pseudo-reference electrode. Similarly, another variant of cell 2 with a Nafion® membrane was prepared by casting 7 µL of Nafion® mixture onto the ITO SPE. Nafion® mixture was prepared by mixing 90 vol% of 5% Nafion® with 10 vol% of DMF. Both variants of cell 2 are assembled on ITO SPE as it does not contain Pt and has lower non-Faradaic capacitance in comparison with carbon SPE.

III. Soft landing of redox active cluster ions.

Two SL instruments, briefly described in the following section, were used in this study. In the first instrument, shown in Fig. S4 (1), ions are produced using electrospray ionization (ESI) of a 150 µM solution of $Na_3[PMo_{12}O_{40}]$ xH_2O in methanol introduced at a flow rate of 80 µL/hr by a syringe pump (Legato 180, KD Scientific, Holliston, MA, USA). Charged droplets produced by applying -2.5 kV to a pulled four-bore borosilicate glass ESI emitter (VitroCom, NJ, USA) are entrained into the vacuum system using a heated stainless steel inlet where they undergo desolvation. Ions are subsequently transferred through four stages of differential pumping using a dual ion funnel system (Fig. S4) (1) followed by an RF-only collision quadrupole (CQ), a resolving quadrupole mass filter (Extrel CMS, Pittsburgh, PA, USA), and three einzel lenses in series that focus the ion beam onto the deposition target. The first and second ion funnel are maintained at 4 and 0.5 Torr, respectively, while the CQ and RQ are maintained at 2 x 10^{-2} Torr and at 8 × 10^{-5} Torr, respectively during deposition. The kinetic energy of the ions was maintained at 30-35 eV/charge. Additional experiments were performed with lower kinetic energy of 5 eV/charge in order to confirm that POM anions are deposited intact on the cell surface.The ion current on the WE was measured with a picoammeter (model 9103, RBD Instruments, Bend, OR). The total number of ions deposited was calculated by integrating the ion current over time. The ion beam produced by the SL instrument is circular and ~ 2-3 mm in diameter (2). A typical ESI mass spectrum of a $Na_3[PMo_{12}O_{40}]$ solution (Fig. S5) contains stable $PMo_{12}O_{40}^{3-}$ and $HPMo_{12}O_{40}^{2-}$ anions at m/z = 608 and 911, respectively (3, 4), both of which were examined in this study. In addition, the two most abundant complementary fragment ions, $Mo_7O_{22}^{2-}$ (m/z = 512) and $PMo_5O_{18}^{-}$ (m/z = 798), produced by in-source CID of $PMo_{12}O_{40}^{3-}$ (Fig. S6) (3) were mass selected and deposited onto the in situ IL cell. In CID, molecular ions are accelerated by electric fields and fragment ions are generated through energetic collisions of precursor ions with neutral gas molecules. In this study, in-source CID was achieved by increasing the RF frequency of both ion funnels and adjusting the potential difference between the end plate of the second ion funnel and the DC offset of the CQ.

IV. Soft landing of bare Pt cluster ions.

A detailed description of the gas-phase synthesis and SL of bare anionic Pt clusters is provided in previous publications (5, 6). Briefly, the modified commercial Nanogen-Trio cluster

source and Q-Prep 500 deposition system (Mantis Deposition Ltd, Oxfordshire, U.K.) were used in this study. Bare Pt clusters were prepared by DC magnetron sputtering of a circular Pt target (1″ diameter, 0.15″ thick, 99.95% purity, Plasmaterials, Livermore, CA, USA) in a controlled flow of ultra-high purity (UHP) argon and helium (99.999% purity, Matheson Tri-Gas, Newark, CA, USA). The sputtering current applied to the Pt target, the flow rates of argon and helium, and the position of the linear translator in the aggregation region were adjusted to optimize the production (total anion current) of the Pt clusters. After exiting the gas aggregation region, the anionic Pt clusters pass through a skimmer and into a 440 kHz resolving quadrupole mass filter (Extrel, Pittsburgh, PA, USA). The peak of the anionic Pt cluster distribution was maintained at ~6000 amu corresponding to ~Pt_{30} and a cluster size of ~1 nm. The quadrupole mass filter was operated in RF only mode to allow a focused distribution of anionic Pt clusters to deposit on cell 2.

V. Electrochemical experiments using cell 1 and 2

The electrochemical characteristics of the in situ IL cells (cell 1 and 2) and redox behavior of the internal reference redox Cc/Cc^+ couple in cell 1 were evaluated using cyclic voltammetry (CV) and electrochemical impedance spectroscopy (EIS). The stability of the IL membrane of cell 1 in vacuum (~10^{-5} Torr) was examined by acquiring CVs at different time intervals. These experiments allowed us to examine water evaporation from cell 1 and expand the operating potential range over time. After complete removal of water, which typically takes more than 8 hours in vacuum at room temperature, the cell could be operated in a wide potential range of -1800 - 1000 mV vs. Ag. CVs were acquired at different scan rates (5, 10, 20, 50, 100, 200, 400 mV/ s). For cell 1, the potential ranges of -1000 to 1000 mV and -1800 to -1000 mV were used to evaluate the electrical double layer (EDL) charge-discharge and redox activity of the Cc/Cc^+ redox couple, respectively. For both cells 1 and 2 with IL, EIS was performed to examine the resistance across different interfacial regions. In EIS, a sinusoidal perturbation with an amplitude of 10 mV and frequency in a range of 100 KHz to 1 Hz is applied to the electrochemical cell and the impedance across the circuit is measured as a function of the frequency. For cell 2 with Nafion®, the higher frequency limit was increased to 1 MHz. Therefore a sinusoidal perturbation with an amplitude of 10 mV and frequency in a range of 1

MHz to 1 Hz is applied to measure the EIS spectra of this cell. The EIS spectra were analyzed using EIS Spectrum Analyzer 2.0 (7).

Redox electrochemistry was examined by soft-landing ~1 x 10^{14} POM ions at a kinetic energy of either 5 or 30 eV/charge onto cell 1 and acquiring CVs between -1700 and 1000 mV at different scan rates. CVs presented in the main manuscript were acquired after soft-landing POM anions at a kinetic energy of 30 eV/charge whereas CVs of POM soft landed at 5 eV/charge are presented in Figure S11. CVs showed distinguishable redox peaks of both the internal reference redox couple - Cc/Cc^+ and the SL analyte. Since the metallic Ag RE may also undergo additional electrode polarization upon addition of the redox active SL ions, the obtained CV curves were shifted manually in the data processing step to maintain the reduction potential of Cc/Cc^+ at the value of -1520 mV observed before SL. Of note, softlanded POM anions studied in this work have several isomeric structures. The α-Keggin anion is the most stable isomer of $PMo_{12}O_{40}$. The α-isomer is known to be ~5 kcal/mol less stable than the β-Keggin anion(8). The α-isomer is converted into β-isomer almost quantitatively after 2-3 reductions (9). Although it is unlikely that the soft landed $PMo_{12}O_{40}$ anions adopt several isomeric structures, it is reasonable to assume that other isomers are formed during CV. In contrast, fragments of $PMo_{12}O_{40}$ formed using in-source CID are most likely present in several isomeric forms. Different isomeric structures may exhibit slight changes in the levels of the highest occupied and lowest unoccupied molecular orbitals (HOMO-LUMO) as reported in the literature, which in turn may result in different redox behavior (10). For this study, it is assumed that the redox activity of POM anions is a result of the collective behavior originating from the most stable isomers of soft landed POMs. The relative stability of particular isomers of a specific cluster depends on the charge of the cluster and its interaction with the support (10). Since the charge on the cluster changes at each redox step during electrochemical cycling, it is reasonable to assume that interconversions between isomers occur during CV measurements. The characterization of isomeric structures of POM anions upon soft landing and during electrochemical cycling is extremely challenging given the complex nature of the EEI which contains both electrolyte ions and POM anions and is beyond the scope of this study.

Reactive electrochemistry was examined by placing cell 2 containing a protic IL membrane inside the vacuum region of the magnetron sputtering soft landing instrument. After deposition of bare Pt clusters directly onto cell 2, it was moved to a second vacuum chamber

fitted with an ultra-high purity N_2 and O_2 inlet. Initially, CVs were acquired between -1000 and 1500 mV in the chamber filled with N_2 gas and subsequently with O_2 to evaluate hydrogen adsorption/desorption and ORR, respectively. All CV and EIS experiments for both redox and reactive electrochemistry were repeated at least 5 times. Similar deposition experiments were performed on the cell containing a Nafion® membrane. Bare Pt clusters were directly deposited onto the cell and moved to a second chamber fitted with an humidified N_2 and O_2 inlet. Nafion® conducts protons only when it is humidified, therefore the second chamber was completely humidified during electrochemical measurements. Cell 2 with Nafion® was kept inside the humidified chamber for 2 hours before electrochemical measurements to achieve a complete saturation of Nafion® and obtain reproducible CVs. The source of protons for the ORR in latter case comes from Nafion® itself. Hydrogen evolution followed by further dissociation to generate protons takes place during every CV scan below 0 V. Prior to every electrochemical measurement using cell 1 and 2, the uncompensated ohmic potential drop was measured using EIS and it was found to be negligible(usually below 1-3 mV). Therefore the measured potential or current values are not affected by any uncompensated ohmic potential drop in the cells.

VI. Development and optimization of in-situ cells

The working in-situ cells were developed through the minimization of double-layer charge-discharge capacitive current (non-Faradaic) and optimization of IL membrane thickness to facilitate the efficient transport of soft-landed (SL) analyte and reactant gases from the top surface layer of the electrolyte to the WE surface. Initially, the concentration of IL electrolyte ions in the membrane was optimized to reduce the non-Faradaic capacitive current. Based on the IL electrolyte concentration used in this study, the non-Faradaic capacitance on WE of ~ 16 μC for BF_4^- (anodic scan) and ~9 μC for $EMIM^+$ (cathodic scan) was calculated theoretically by estimating the number of electrolyte ions that could possibly adsorb on the entire WE using the size of the electrolyte ions and WE surface area. It was assumed that the entire WE surface area was closely packed solely by adsorption of only electrolyte ions (anions during anodic scan and cations during cathodic scan) without solvent molecules to form a perfect double layer. The difference between the cathodic and anodic capacitance reflects the difference in the size of BF_4^- and $EMIM^+$ ions.

In SL experiments, ~1 x 10^{14} redox active ions were immobilized on the surface resulting in ~16 µC of Faradaic capacitance. This value was estimated using Faraday's law and assuming it undergoes at least one electron transfer per ion at EEI. It is noted that the contribution of the Faradaic component from SL ions are at least equal to or higher than the non-Faradaic component. Therefore, it is considered that non-Faradaic capacitance will not suppress the Faradaic component of analyte species even in an ideal case which is important criterion when evaluating the activity of SL ions. Additionally, the IL membrane thickness was adjusted to ~ 10 µm to optimize transport of ions deposited on top of the electrolyte layer to WE surface while not increasing the electrolyte resistance.

Subsequent to optimization of in situ cell fabrication, the electrochemical properties of the in-situ cells such as the stability of EEI and redox activity of the internal redox reference couple (Cc/Cc^+) of cell 1, non-Faradaic capacitances, and interfacial resistances of both cell 1 and 2 were studied. Figure S1 shows CVs obtained at different time points (0, 3, and 6 hrs) after the introduction of cell 1 into the vacuum system of the SL instrument maintained at 10^{-5} Torr. The cell fabricated without vacuum drying showed the presence of hydrogen and oxygen evolution regions at far negative and positive potentials respectively due to electrolysis of residual water. Following slow evaporation of water molecules from the IL membrane, the operating potential range of the cell was substantially expanded (See Fig. S1). It took about ~8 hours for complete removal of water and extension of the potential range of the probe to -1800 mV - +1000 mV, where redox processes of both Cc/Cc^+ and SL ions are observed. CVs measured over two potential ranges after complete evaporation of water from the electrolyte layer at a scan rate of 10 mV s^{-1} are shown in Fig. 2. The CV measured between -1800 mV and -1000 mV showed the $1e^-$ reversible redox process of Cc/Cc^+ with the oxidation and reduction peaks at -1450 mV and -1520 mV vs. Ag, respectively and the formal potential (E_f) at ~1480 mV vs. Ag. The $1e^-$ reversible redox process of Cc/Cc^+ is characterized by the difference in half-wave potential ($E_{1/2}$) and peak potential (E_p) of anodic and cathodic processes at around 60 mV (See Table S1). The CV measured between between -1 V and 1 V vs. Ag in cell 1 (see Fig. 2) and between -1000 mV and 1500 mV vs. Ag showed the typical non-Faradaic charge-discharge behavior of electrolyte ions. These observations demonstrate that the solid IL membrane maintains the characteristic redox behavior of the Cc/Cc^+ redox couple and supports the formation of a stable electric double layer.

Figure S2 (a) shows CVs of Cc/Cc^+ obtained at different scan rates between -1800 mV and -1000 mV for cell 1. A linear increase in peak current with the square root of the scan rate in both oxidation and reduction scans (see Figure S2(a) inlet) observed for the Cc/Cc^+ redox couple is representative of typical Randles-Sevcik behavior of redox ions on the WE and confirms rapid electron transfer kinetics and reversibility of this process occurring at EEI of cell 1. A proportional increase in the non-Faradaic current with increasing scan rate shown in Figure S2(b) further confirms the presence of a stable EEI in cell 1. The diffusion coefficient of 5.1 x 10^{-7} cm^2/s was calculated using the Randles-Sevcik equation (equation S1) for Cc/Cc^+ in IL membrane.

$$i_p = 0.4463\ nFAC\sqrt{\frac{nF\nu D}{RT}} \quad (S1)$$

where, i_p – peak current (A), n – number of electrons transferred, F – Faraday constant (96495 C mol^{-1}), A – Electrode surface area (cm^2), C – concentration of analyte ($mol.cm^{-3}$) , ν – scan rate ($V.s^{-1}$), D – Diffusion coefficient of analyte ($cm^2\ s^{-1}$), R – universal gas constant (8.314 $J\ K^{-1}mol^{-1}$), and T- absolute temperature (K). The calculated value of the diffusion coefficient of the Cc/Cc^+ redox couple in $EMIMBF_4$ is in the same order of magnitude with the values reported in the literature (~ 1.1 x 10^{-7} cm^2/s) for Cc/Cc^+ in pristine $EMIMBF_4$ (11). It is imperative to note that the diffusion coefficient of redox ions has not changed significantly in the porous IL membrane and vacuum conditions employed in this study which establishes the superior mass transfer at EEI in the solid state in-situ cell in comparison to liquid electrochemical cells. Table S1 shows a summary of key electrochemical parameters derived from the data shown in Figure S2(a). The current functions, R_{ox} and R_{red}, defined in Table S1 is a ratio of oxidation ($i_{p,ox}$) and reduction peak currents ($i_{p,red}$) vs. square root of different scan rates ($\nu^{0.5}$), respectively.

A deviation from typical Randles–Sevcik behavior is observed at higher scan rates, which is evidenced by the decrease of current functions R_{ox} and R_{red} listed in Table S1. This decrease was attributed to the decrease in diffusion of redox ions to WE surface caused by substantial increase in adsorption of electrolyte ions at higher scan rates. This conclusion is consistent with the observed increase in non-Faradaic capacitance with a scan rate shown in Figure S2 (b) and a slight increase in E_f (Table S1). Therefore, a majority of CV measurements were performed at a lower scan rate of 10 mV s^{-1} to ensure that these processes do not affect the observed redox

activity of SL ions. The difference in the oxidation and reduction part of the non-Faradaic capacitance of electrolyte ions (as observed in Figure 2 and S2(b)) and Faradaic currents of Cc/Cc^+ redox couple (as observed in Figure S2(a) and current functions in Table S1) is due to the asymmetry of the ion sizes of electrolyte cations ($EMIM^+$) and anions (BF_4^-) respectively (12-14) and subsequently effects the formation of electrical double layers (EDL) during oxidation and reduction scans.

Followed by voltammetry characterization, different interfacial regions in the in-situ cell were examined using EIS for cells 1 and 2. A typical Nyquist plot obtained for cell 1 is shown in Figure S3 (a). The presence of a semicircle observed in the high frequency range (1 kHz −100 kHz) was attributed to the polarization of the WE controlled by charge transfer kinetics. The total impedance in this region is a combination of the electrolyte resistance (R_e), charge transfer resistance R_{ct} and double layer capacitance (C_{dl}). The equivalent circuit is represented by R_e (R_{ct} || C_{dl}).

The frequency range between 1 kHz to 40 Hz and the approximate beeline (a straight line with a slope following the semicircle) present after 40 Hz was attributed to the polarization of the WE controlled by diffusion through the layered IL membrane and thin, porous Pt electrode surface respectively. The presence of porous structure of the IL membrane with thickness of ~10 µm was observed using SEM (Figure 1 (c and d)). The Warburg impedance, usually characterized by beeline, exists at 45^o in the lower frequency region in the infinite diffusion model (15). The presence of a thin, porous Pt electrode surface in cell 1 defines the finite diffusion layer with diffusion of ionic species through pores and therefore the beeline is not at a 45^o angle. Therefore, The total impedance in the lower frequency region is a combination of the porous membrane resistance (R_m), double layer capacitance derived at the porous membrane (C_m), and Warburg impedance ($Z_{w,o}$). The finite length diffusion with the reflective boundary condition exist for Warburg impedance $Z_{w,o}$ and reflects that the further adsorption of ionic species on Pt WE surface is not possible most likely due to the presence of highly concentrated IL at the surface. The equivalent circuit of the observed impedance region and the best fit obtained using this model are shown in Figure S3(c) and S3(a) respectively. Note the constant phase element has been introduced in an equivalent circuit instead of the pure capacitive element to account for the fact that the double layer capacitance is not ideal and characterized by the presence of porous Pt surface. The increase in impedance in the frequency region below 40 Hz

indicates the absence of further adsorption of ionic species on WE. The experimental impedance data were fitted using EIS spectrum analyzer software. The equivalent circuit model presented in Figure S3 (c) was used in the fitting process. The values of fitted parameters are C_{dl} = 1.24 x 10^{-8} F, C_m = 5.0 x 10^{-4} F, R_e=167 Ω, R_{ct} = 1972 Ω, R_m = 9.8 x 10^5 Ω, $Z_{w,o}(r)$ = 2.2 x 10^4 Ω $s^{-0.5}$ and $Z_{w,o}(c)$ = 0.13 m. $s^{0.5}$. Assuming the diffusion of oxidized and reduced species are the same, the diffusion coefficients of ions in the electrolyte layer and the Nernst diffusion layer thickness were calculated using equations S2-S4:

$$Z_{w,o}(\omega) = \frac{Z_{w,o}(r)}{\sqrt{\omega}}\,(1-j)\coth(Z_{w,o}(c)\sqrt{j\omega}) \quad \text{(S2)}$$

$$Z_{w,o}(r) = \frac{RT}{n^2F^2A\sqrt{2}}\left[\frac{1}{\sqrt{D_O}C_{S,O}} + \frac{1}{\sqrt{D_R}C_{S,O}}\right] \quad \text{(S3)}$$

$$Z_{w,o}(c) = \frac{d}{\sqrt{D}} \quad \text{(S4)}$$

where, $Z_{w,o}(\omega)$ is the impedance of finite-length diffusion with reflective boundary, $Z_{w,o}(r)$ (Ω $s^{-0.5}$) and $Z_{w,o}(c)$ (m. $s^{0.5}$) are parameters of $Z_{w,o}(\omega)$, D_O and D_R – diffusion coefficients of oxidized and reduced species (m^2/s) (we assume, D_O = D_O = D), $C_{S,O}$ and $C_{S,R}$ – surface concentrations of oxidized and reduced species, d – the Nernst diffusion layer thickness.

Using an electrode surface area of 7 x 10^{-6} m^2, the diffusion coefficient of ~6.3 x 10^{-7} cm^2/s and the Nernst diffusion layer thickness of ~100 nm were obtained. The estimated diffusion coefficient is comparable to the value of 5.1 x 10^{-7} cm^2/s calculated using the Randles-Sevcik equation, which corroborates the analysis of the EIS data. The Nernst diffusion layer thickness is well below the total thickness of the IL (~10 µm). The impedance analysis indicates efficient diffusion of ions in the IL membrane in cell 1. It follows that ions deposited on the top surface of the IL membrane readily diffuse to the electrode surface to participate in redox processes. Therefore the electrochemical measurements in thin film cells developed in this study mimic those in liquid cells.

Following the characterization of cell 1, the impedance of different interfacial regions and diffusion properties of cell 2 with IL and Nafion® membrane were characterized using EIS. Prior to Pt cluster deposition, cell 2 with IL was introduced into the vacuum system of the instrument using a vacuum lock system and EIS was performed under vacuum (~ 10^{-7} Torr) to study the properties of different interfacial regions in cell 2 and ensure the stability of the proton-

conducting IL membrane in vacuum during deposition. In case of cell 2 with Nafion® membrane, EIS under vacuum cannot be performed since Nafion® requires humidification for ionic conduction. Therefore, EIS of cell 2 with Nafion® was performed in loading chamber filled with humidified N_2. The experimental impedance data were fitted using EIS spectrum analyzer software. The equivalent circuit model presented in Figure S3(c) was used in the fitting process. The experimental and simulated EIS curves for cell 2 with IL and Nafion® are shown in Figure S3(b1) and (b2) respectively. The best fit for cell 2 with IL was obtained using the following values of fitting parameters: C_{dl} = 1.16 x 10^{-8} F, C_m = 2.2 x 10^{-6} F, R_e =138 Ω, R_{ct} = 846 Ω, R_m = 1 x 10^6 Ω, $Z_{w,o}(r)$ = 2.8 x 10^4 Ω $s^{-0.5}$ and $Z_{w,o}(c)$ = 9.63 m. $s^{0.5}$. Similarly for cell 2 with Nafion®, the values are C_{dl} = 5.23 x 10^{-10} F, C_m = 2.0 x 10^{-6} F, R_e =0.15 Ω, R_{ct} = 3330 Ω, R_m = 1690 Ω, $Z_{w,o}(r)$ = 7.0 x 10^4 Ω $s^{-0.5}$ and $Z_{w,o}(c)$ = 0.1 m. $s^{0.5}$.

Assuming similar diffusion of oxidized and reduced species, we calculated the diffusion coefficient of 7.56 x 10^{-7} cm^2/s for ions in the electrolyte layer of cell 2 with IL and the Nernst diffusion layer thickness of ~2.6 μm using equations S2-S4. For cell 2 with Nafion®, the diffusion coefficient and the Nernst diffusion layer thickness are estimated to be 2.5 x 10^{-8} cm^2/s and 24 nm, respectively. The diffusion coefficient of 7.56 x 10^{-7} cm^2/s observed for the proton-conducting IL membrane is of the same order in comparison to the diffusion coefficient determined for typical protic membrane used in commercial PEMFCs (for example, 5 x 10^{-7} cm^2/s for Nafion®(16)). The decrease in the double layer capacitance, electrolyte and charge transfer resistance on the electrode surface, and porous proton conducting IL membrane in cell 2 compared to cell 1, was attributed to a lower surface area of ITO WE and higher occupancy smaller size H^+ ions at the surface and further facilitated the ionic diffusion on cell 2. The increased ionic diffusion was also accompanied by an increase in diffusion layer thickness compared to cell 1. On the other hand, the diffusion coefficient of the Nafion® membrane is lower than the literature values, which is attributed to lower thickness of the Nafion® membrane used in this study or an insufficiently humidified membrane. The thickness of Nafion® was initially optimized and kept at a minimum so that deposited Pt clusters may diffuse through the membrane to reach the electrode surface. Additionally, the diffusion layer of the Nafion® containing cell 2 is very small compared to the IL containing probe, which indicates that the probe may exhibit reduced mass transport of reactants to the interface. Nevertheless, our proof-

of-concept experiments demonstrate the feasibility of soft-landing and electrochemical characterization of ORR activity of bare Pt clusters on both membranes.

VII. Estimation of the electrochemically active surface area of bare Pt clusters

The electrochemically active surface area (ECSA) of 37.8 m^2/g_{Pt} was calculated for cell 2 with IL membrane using Eq. S5:

$$\mathrm{ECSA}\left(\frac{m_{Pt}^2}{g_{Pt}}\right) = \frac{q_{Pt}}{q_P^o . m_{Pt}} \quad \text{(S5)}$$

where, q_{Pt} – total charge accumulated during H^+ desorption, q_P^o - charge due to adsorption of one monolayer of H^+ on Pt = 0.210 mC/cm^2, m_{Pt} - Pt loading (~2.5 x 10^{-6} mg_{Pt} /cm^2).

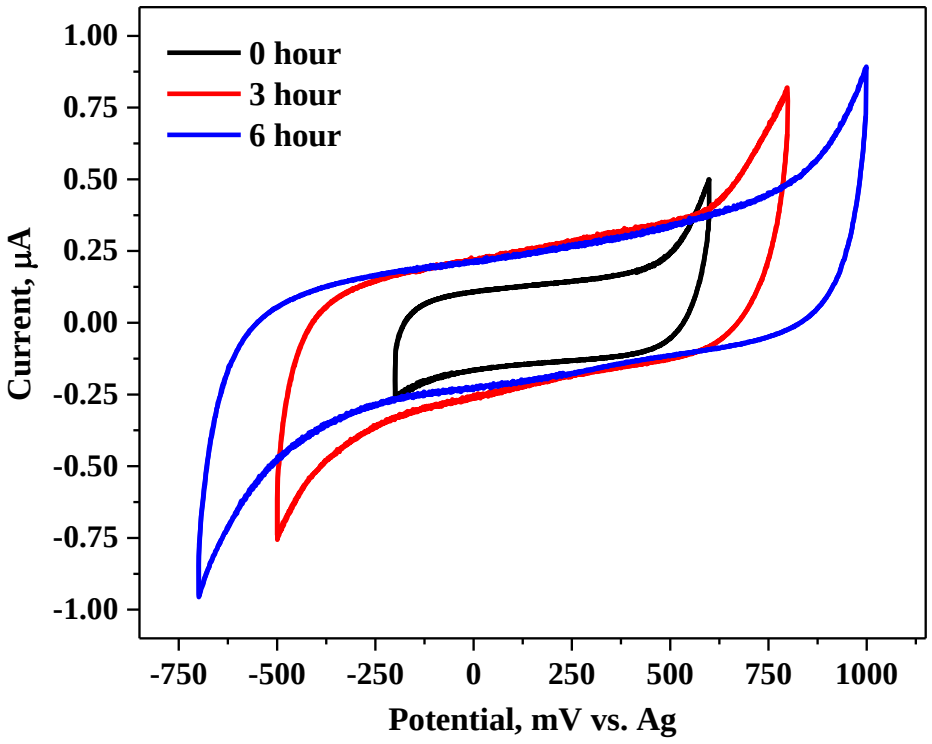

Fig. S1. CVs of cell 1 acquired at different time intervals at 10^{-5} Torr and varying potential ranges. Scan rate: 10 mV s^{-1}.

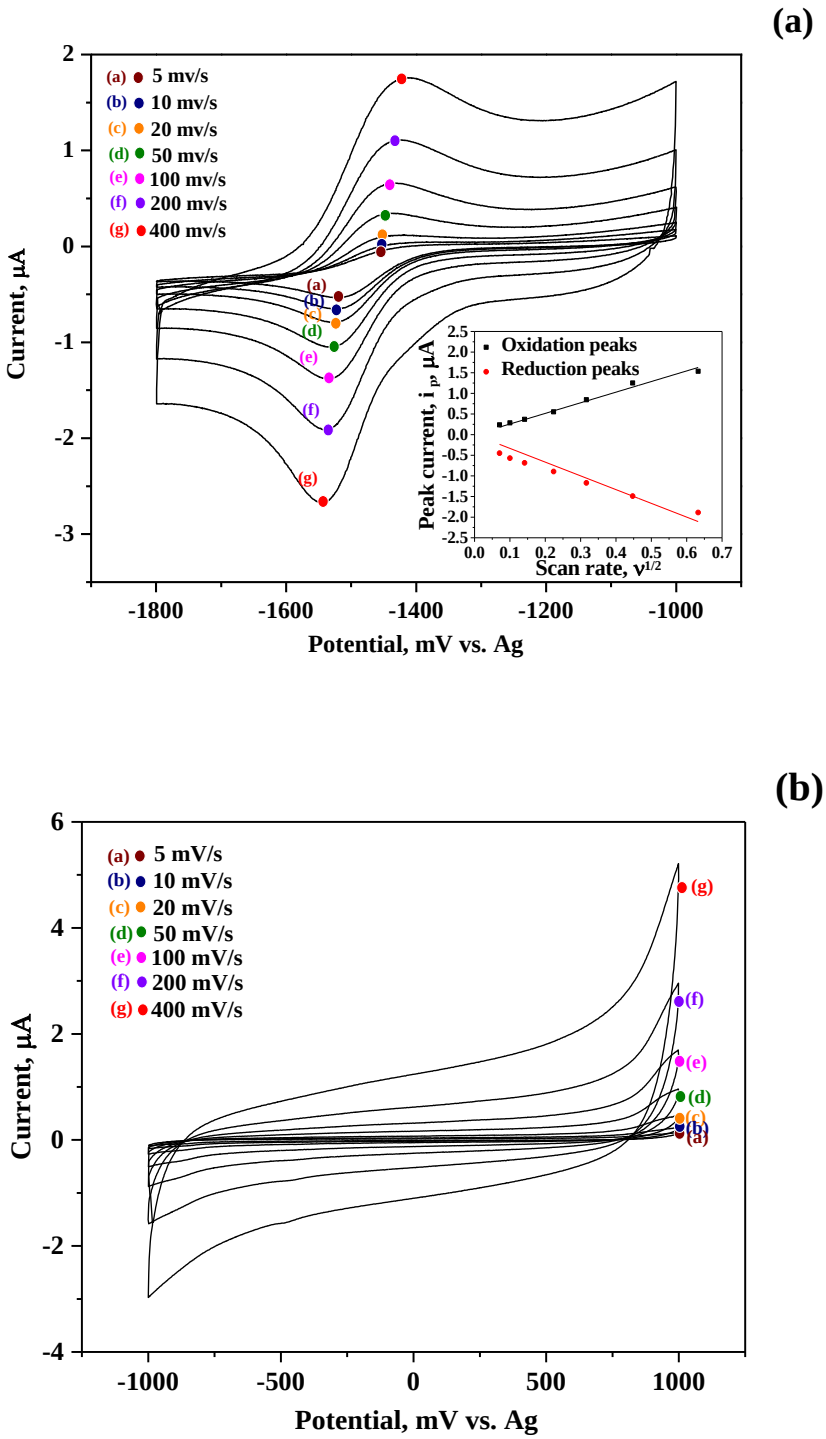

Fig. S2. CVs of cell 1 acquired at different scan rates (5, 10, 20, 50, 100, 200, and 400 mVs^{-1}) **(a)** to represent a redox (Faradaic) behavior of Cc/Cc^{+} observed between -1800 and -1000 mV vs. Ag and **(b)** to represent typical electrical double layer (non-Faradaic) behavior observed between -1000 mV and 1000 mV vs. Ag.

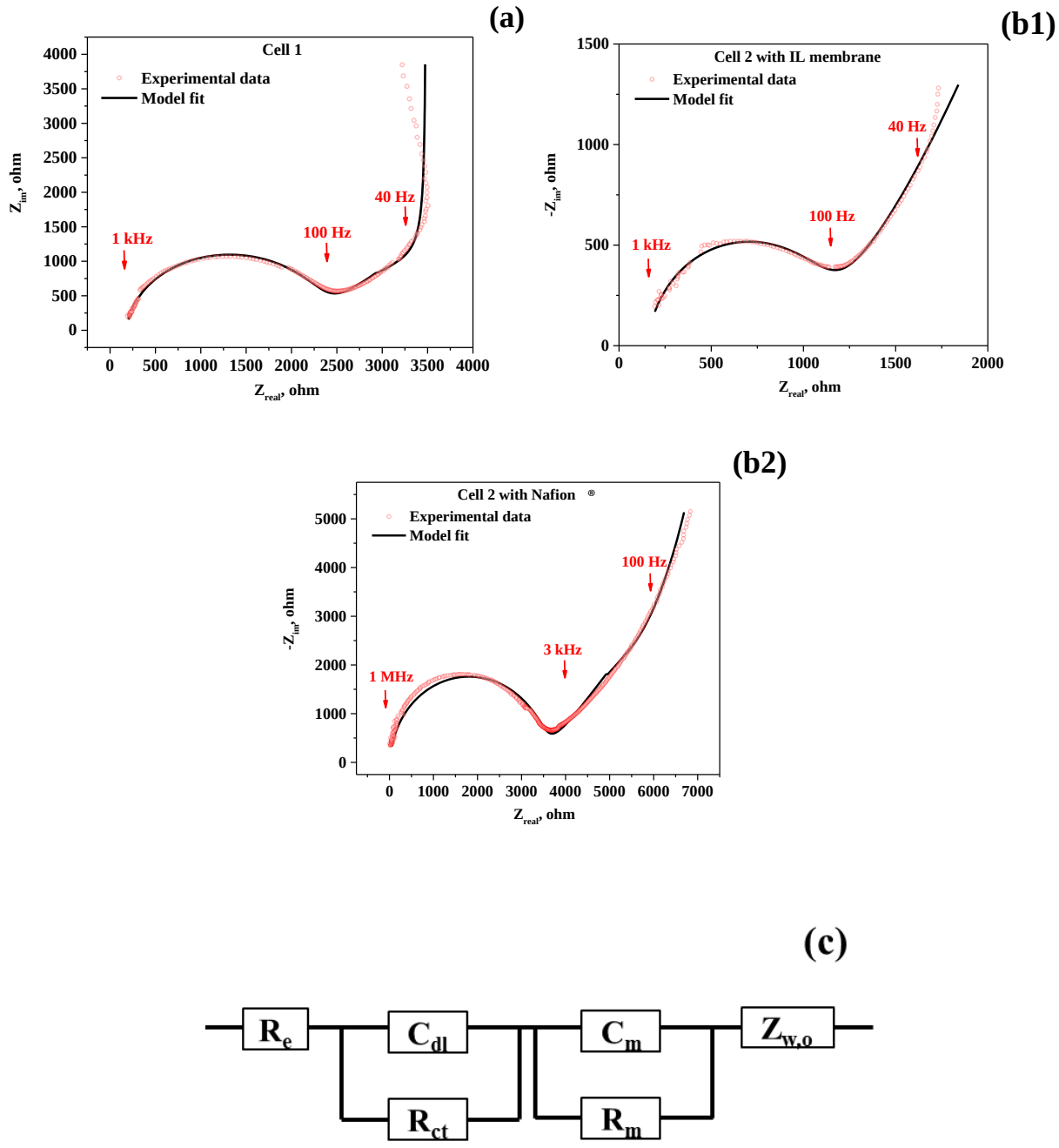

Fig. S3. Nyquist plots obtained from the potentiostatic EIS of cell 1 **(a)**, cell 2 with IL membrane **(b1)** and cell 2 with Nafion® **(b2)** (frequency range: 100 KHz to 1 Hz, amplitude: 10 mV; for b2, frequency range: 1 MHz to 1 Hz); **(c)** the equivalent circuit model used to fit the EIS data presented in (a) and (b) (R_e -electrolyte resistance, R_{ct} - charge transfer resistance, C_{dl} - double layer capacitance, R_m - porous membrane resistance, C_m-double layer capacitance derived at porous membrane, and $Z_{w,o}$-Warburg impedance).

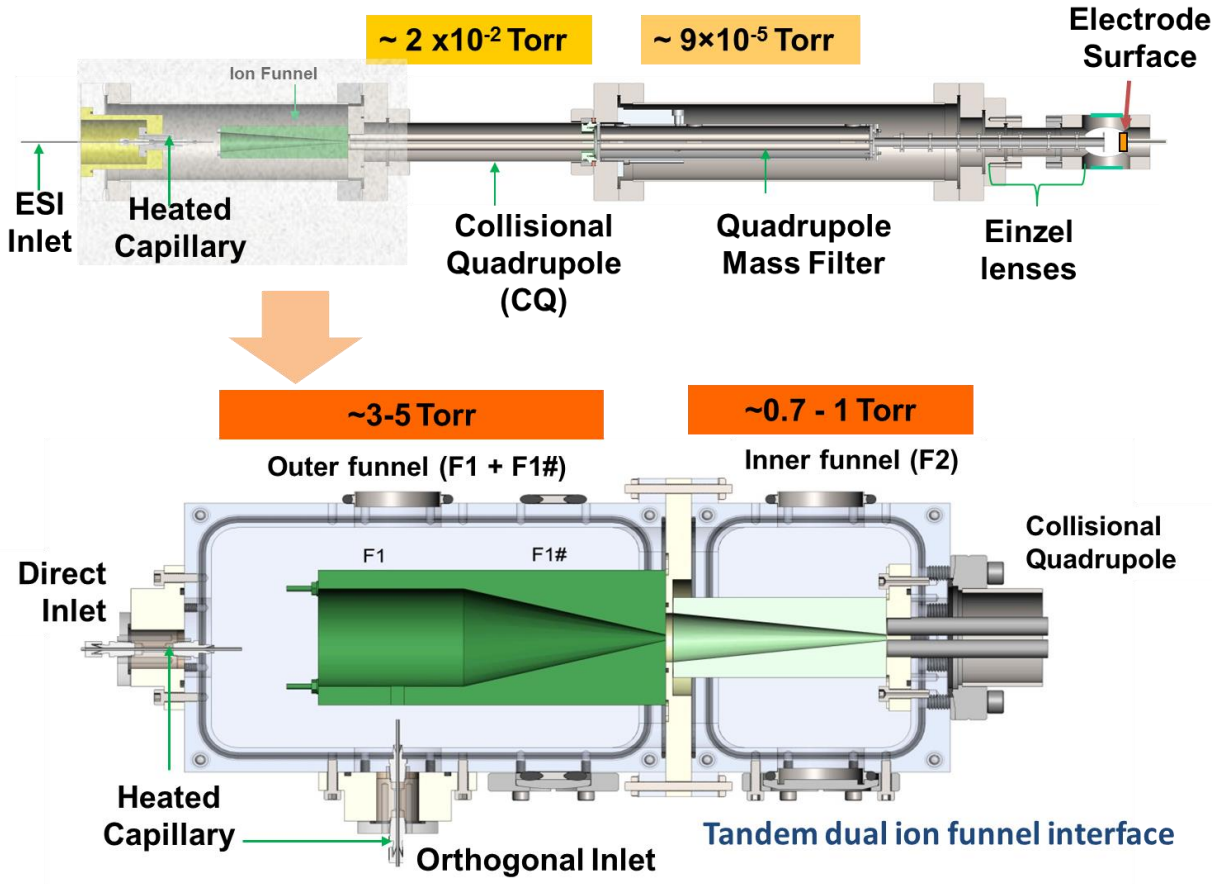

Fig. S4. Schematic diagram of the high flux ion soft-landing instrument used to deposit mass- and charge- selected ions in this study.(1)

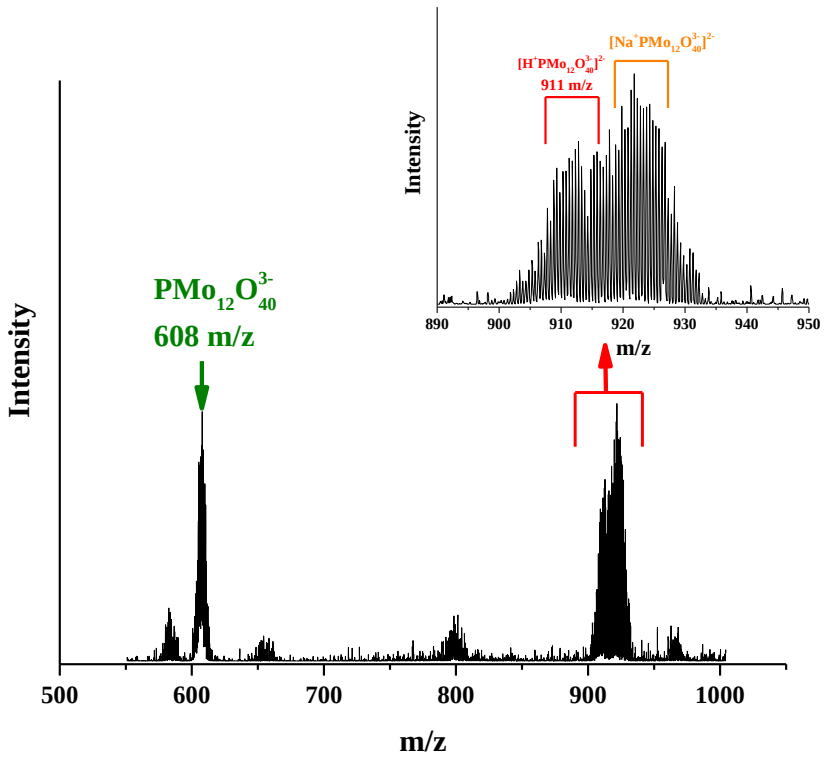

Fig. S5. Representative mass spectrum obtained by electrospray ionization of the $Na_3(PMo_{12}O_{40})$ x H_2O showing the presence of triply charged POM anion ($PMo_{12}O_{40}^{3-}$) and two types of doubly charged anions such as $[H^+PMo_{12}O_{40}^{3-}]^{2-}$ and $[Na^+PMo_{12}O_{40}^{3-}]^{2-}$.

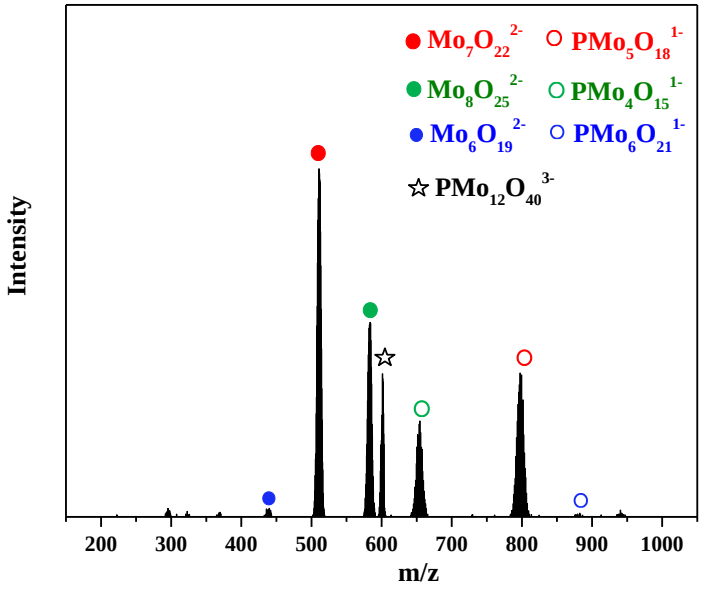

Fig. S6. Representative mass spectrum obtained by collision-induced dissociation of $PMo_{12}O_{40}^{3-}$ anion produced using the smart fragmentation option of the Bruker HCT-ultra ion trap mass spectrometer, in which the excitation amplitude was varied.

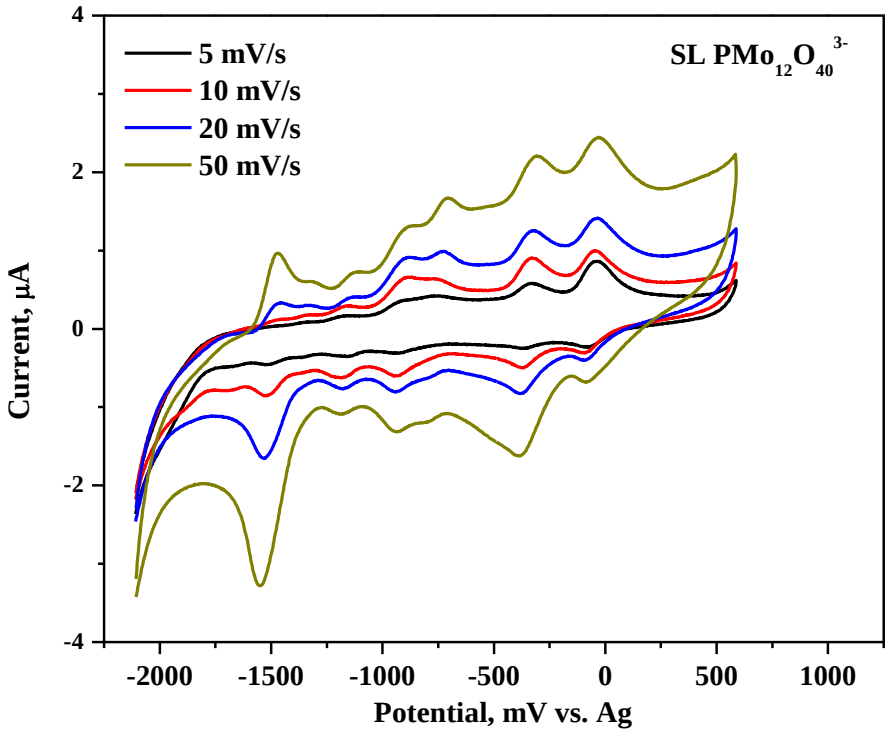

Fig. S7. CVs of cell 1 with soft landed $PMo_{12}O_{40}^{3-}$ at different scan rates (5, 10, 20 and 50 mV s^{-1}). Approximately 1 x 10^{14} ions were deposited.

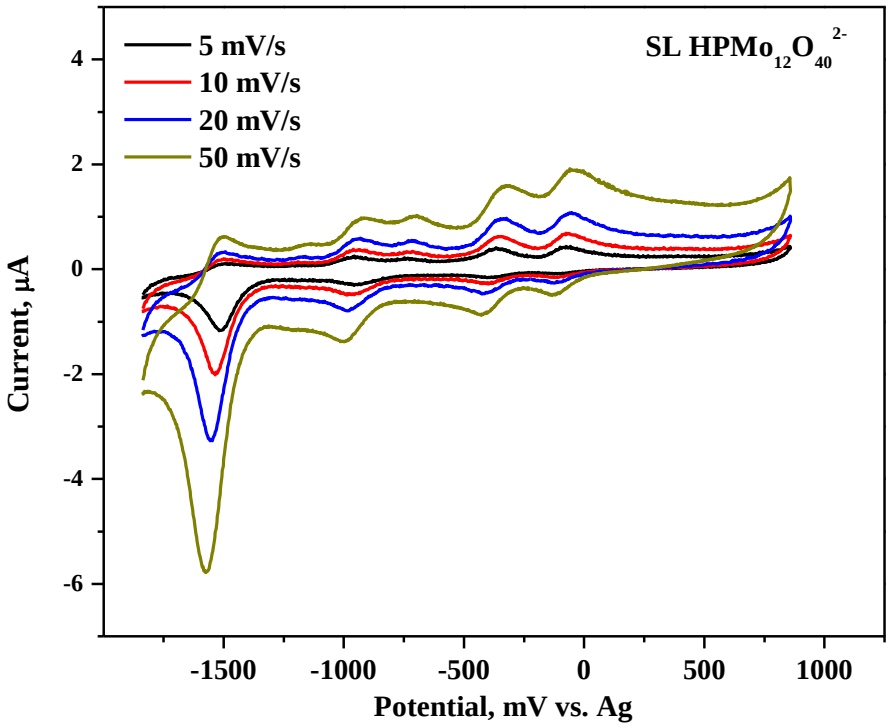

Fig. S8. CVs of cell 1with soft landed $HPMo_{12}O_{40}^{2-}$ at different scan rates (5, 10, 20 and 50 mV s^{-1}). Approximately 1 x 10^{14} ions were deposited.

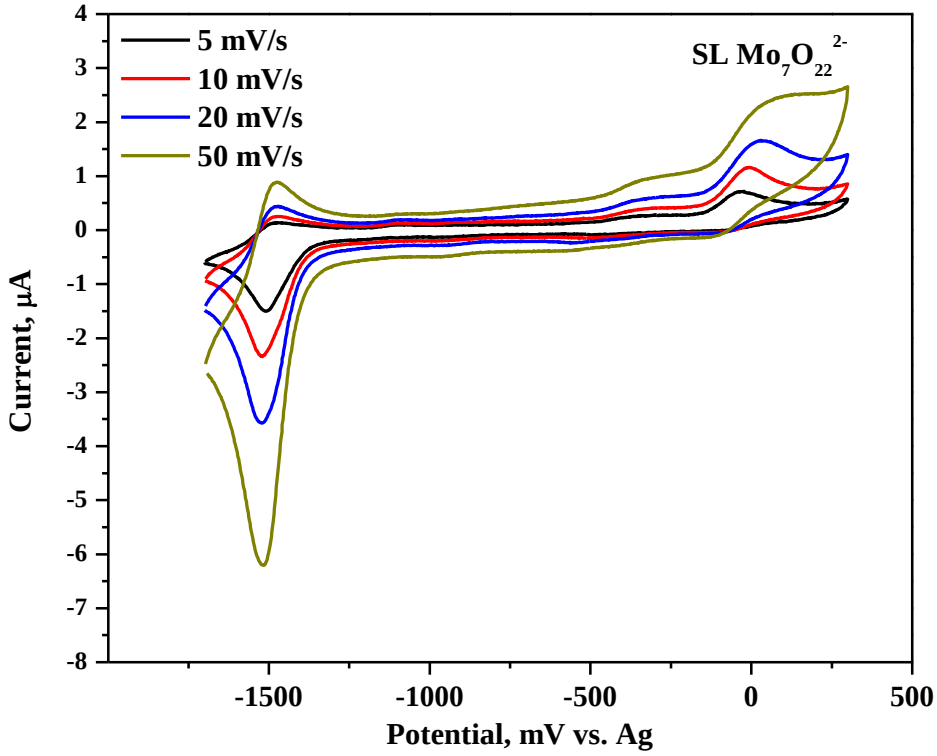

Fig. S9. CVs of cell 1 with soft landed $Mo_7O_{22}^{2-}$ at different scan rates (5, 10, 20 and 50 mV s^{-1}). Approximately 1 x 10^{14} ions were deposited.

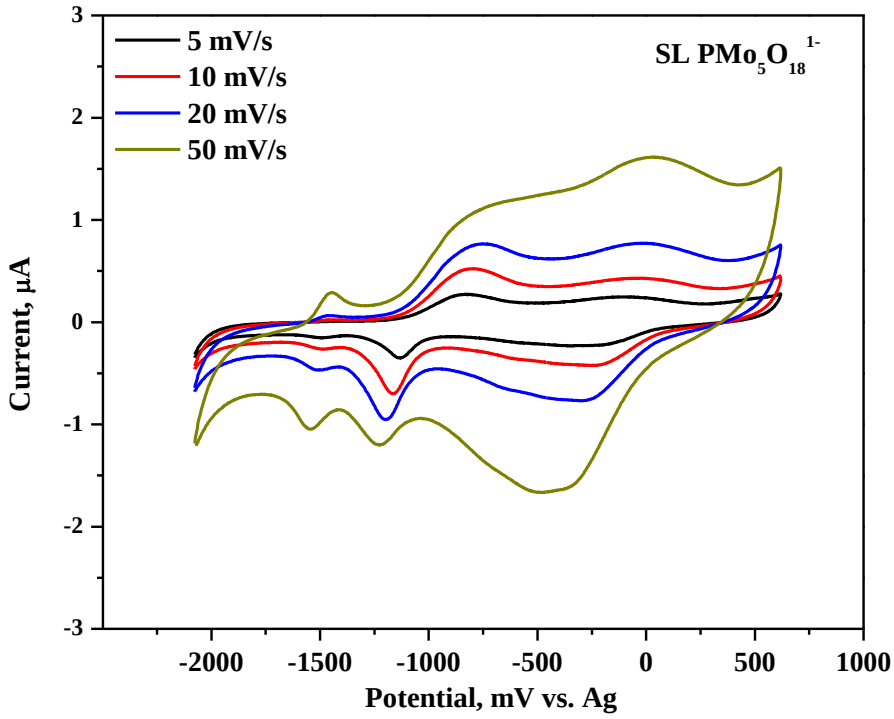

Fig. S10. CVs of cell 1 with soft landed $PMo_5O_{18}^-$ at different scan rates (5, 10, 20 and 50 mV s^{-1}). Approximately 1 x 10^{14} ions were deposited.

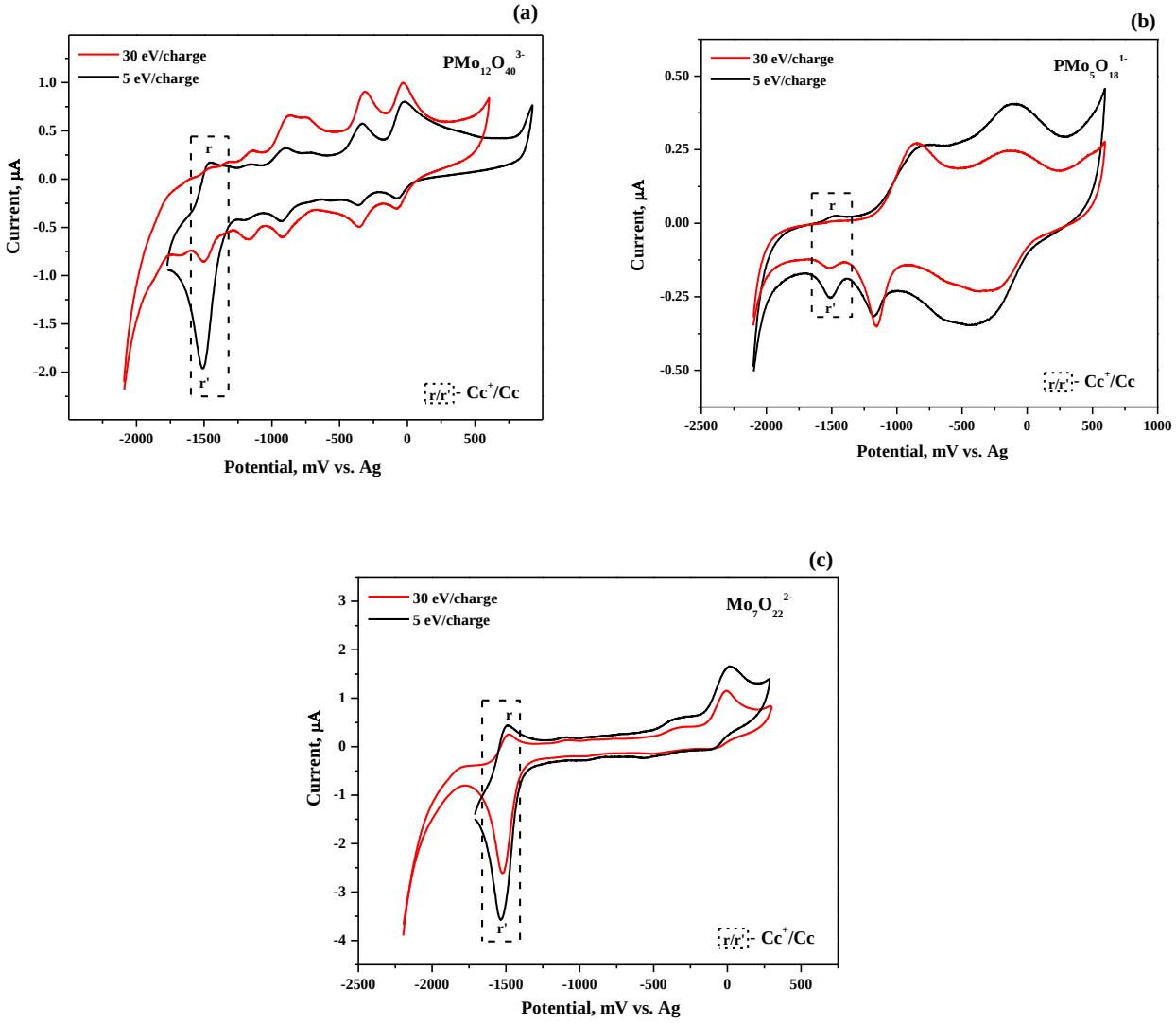

Fig. S11. CVs of cell 1 containing POM anions soft landed at two different kinetic energies (5 eV/charge and 30 eV/charge) with (a) $PMo_{12}O_{40}^{3-}$, (b) $PMo_5O_{18}^{-}$ and (c) $Mo_7O_{22}^{2-}$ at 10 mV s^{-1}. Approximately 1 x 10^{14} ions were deposited in each case.

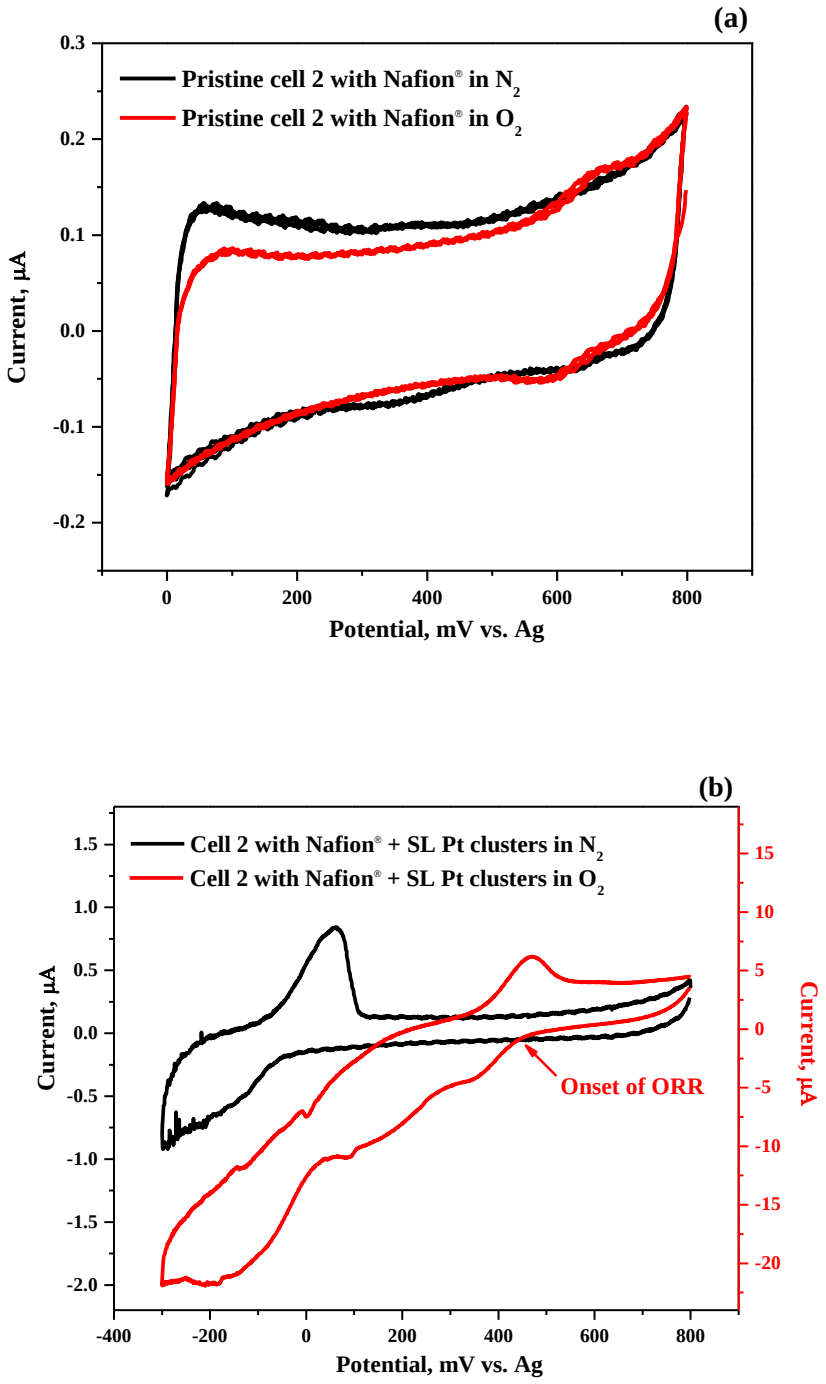

Fig. S12. CVs of (a) pristine cell 2 with Nafion® and (b) cell 2 containing 1×10^{12} soft-landed bare Pt clusters acquired under N_2 and O_2 atmosphere. ORR activity is observed for only for the cell containing soft-landed Pt clusters in O_2. Scan rate: 50 mV s^{-1}.

Table S1: Estimated electrochemical parameters for Cc/Cc^{+} studied using cell 1.

Cc/Cc+	**Oxidation**		**Reduction**		**E_f, mV**
Scan rate, mVs^{-1}	**R_{ox}, $A/(V/s)^{-0.5}$**	**$\Delta(E_{1/2,ox} - E_{p,ox})$, mV**	**R_{red}, $A/(V/s)^{-0.5}$**	**$\Delta(E_{1/2,red} - E_{p,red})$, mV**	
5	335	69	636	60	-1465
10	285	67	570	65	-1469
20	262	66	483	67	-1483
50	247	68	399	64	-1484
100	267	65	369	62	-1485
200	279	80	333	68	-1482
400	242	85	298	69	-1480

Note: Current function, $\mathbf{R_{ox}} = (i_{p,ox}/\sqrt{\nu})/10^{-8}$ and $\mathbf{R_{red}} = (i_{p,red}/\sqrt{\nu})/10^{-8}$, where $i_{p,ox}$ and $i_{p,red}$ – are oxidation and reduction peak currents respectively (A), ν –scan rate (V/s); $E_{1/2,ox}$ and $E_{1/2,red}$ – oxidation and reduction half-wave peak potentials; $E_{p,ox}$ and $E_{p,red}$ are the oxidation and reduction peak potentials, Formal potential, $E_f = (E_{p,ox} + E_{p,red})/2$.

Table S2: Estimated electrochemical parameters for $PMo_{12}O_{40}^{3-}$ and $HPMo_{12}O_{40}^{2-}$ studied using cell 1.

Analyte	Peak #	Oxidation			Reduction			E_f, mV	Number of electron transferred, n
		$E_{p,ox}$, mV	$\Delta(E_{1/2,ox} - E_{p,ox})$, mV	R_{ox}, $A/(V/s)^{-0.5}$	$E_{p,red}$, mV	$\Delta(E_{1/2,red} - E_{p,red})$, mV	R_{red}, $A/(V/s)^{-0.5}$		
$PMo_{12}O_{40}^{3-}$	1	-64	46	234	-90	43	120	-77	1
	2	-350	46	226	-380	50	152	-365	1
	3	-765	29	152	-810	27	40	-788	2
	4	-921	55	203	-950	55	132	-936	1
	5	-1170	48	51	-1173	35	71	-1172	1
	6	-1354	29	6	-1363	17	31	-1359	2
	7	-1639	38	8	-1690	32	16	-1665	1
	8	-1800	85	7	-1890	33	9	-1845	1
$PMo_{12}O_{40}^{2-}$	1	-67	43	244	-90	43	67	-79	1
	2	-353	51	239	-385	44	88	-369	1
	3	-717	25	82	-740	32	43	-729	2
	4	-960	40	139	-950	66	132	-955	1
	5	-1184	35	14	-1165	35	28	-1175	2

Note: $E_{p,ox}$ and $E_{p,red}$ - oxidation and reduction peak potentials; $E_{1/2,ox}$ and $E_{1/2,red}$ – oxidation and reduction half-wave peak potentials; Current function, $R_{ox} = (i_{p,ox}/\sqrt{\nu})/10^{-8}$ and $R_{red} = (i_{p,red}/\sqrt{\nu})/10^{-8}$, where $i_{p,ox}$ and $i_{p,red}$ – oxidation and reduction peak currents respectively (A), ν –scan rate (V/s); Formal potential, $E_f = (E_{p,ox} + E_{p,red})/2$.

Table S3: Estimated electrochemical parameters for primary CID fragments $Mo_7O_{22}^{2-}$ and $PMo_5O_{18}^{1-}$ studied using cell 1.

Analyte	Anodic scan (oxidation)				Cathodic scan (reduction)			
	Peak #	**$E_{p,ox}$, mV**	**$\Delta(E_{1/2,ox} - E_{p,ox})$, mV**	**R_{ox}, A/(V/s)$^{-0.5}$**	**Peak #**	**$E_{p,red}$, mV**	**$\Delta(E_{1/2,red} - E_{p,red})$, mV**	**R_{red}, A/(V/s)$^{-0.5}$**
$Mo_7O_{22}^{2-}$	1	0	77	404	1	-61	48	89
	2	-351	66	45	1”	-419	16	8
	3	-529	7	5	2	-507	22	25
	4	-641	16	2	3	-670	21	2
	5	-777	16	4	4	-790	18	4
	6	-845	16	2	5	-882	15	3
	7	-927	30	7	6	-948	24	4
	8	-1111	29	25	7	-1184	25	5
	9	-1254	16	4		-	-	-
	10	-1832	43	72		-	-	-
$PMo_5O_{18}^{1-}$	1	-46	229	66	1	-233	113	164
	2	-877	142	175	2	-450	65	16
		-	-	-	3	-659	65	7
		-	-	-	4	-860	33	288
		-	-	-	5	-1197	48	21

Note: **$E_{p,ox}$** and **$E_{p,red}$** - oxidation and reduction peak potentials; **$E_{1/2,ox}$** and **$E_{1/2,red}$** – oxidation and reduction half-wave peak potentials; Current function, **R_{ox}** = $(i_{p,ox}/\sqrt{\nu})/10^{-8}$ and **R_{red}** = $(i_{p,red}/\sqrt{\nu})/10^{-8}$, where $i_{p,ox}$ and $i_{p,red}$ – oxidation and reduction peak currents respectively (A), ν –scan rate (V/s); Formal potential, **E_f** = $(E_{p,ox} + E_{p,red})/2$.

References

1. Gunaratne KDD, *et al.* (2015) Design and performance of a high-flux electrospray ionization source for ion soft landing. *Analyst* 140(9):2957-2963.
2. Johnson GE, Hadjar O, & Laskin J (2011) Characterization of the Ion Beam Focusing in a Mass Spectrometer Using an IonCCD™ Detector. *Journal of The American Society for Mass Spectrometry* 22(8):1388-1394.
3. Gunaratne KD, Prabhakaran V, Johnson G, & Laskin J (2015) Gas-Phase Fragmentation Pathways of Mixed Addenda Keggin Anions: PMo12-nWnO40 3– (n = 0–12). *Journal of The American Society for Mass Spectrometry* 26(6):1027-1035.
4. Gunaratne KDD, *et al.* (2014) Controlling the Charge State and Redox Properties of Supported Polyoxometalates via Soft Landing of Mass-Selected Ions. *The Journal of Physical Chemistry C* 118(48):27611-27622.
5. Johnson GE, Colby R, Engelhard M, Moon D, & Laskin J (2015) Soft landing of bare PtRu nanoparticles for electrochemical reduction of oxygen. *Nanoscale* 7(29):12379-12391.
6. Johnson GE, Colby R, & Laskin J (2015) Soft landing of bare nanoparticles with controlled size, composition, and morphology. *Nanoscale* 7(8):3491-3503.
7. Bondarenko AS & Ragoisha GA (2005) In Progress in Chemometrics Research. *In Progress in Chemometrics Research*, ed Pomerantsev AL (Nova Science Publishers, New York), pp 89–102.
8. López X, Bo C, Poblet J-M, & Sarasa JP (2003) Relative Stability in α- and β-Wells−Dawson Heteropolyanions: A DFT Study of [P2M18O62]n- (M = W and Mo) and [P2W15V3O62]n. *Inorganic Chemistry* 42(8):2634-2638.
9. Chiang M-H, Dzielawa JA, Dietz ML, & Antonio MR (2004) Redox chemistry of the Keggin heteropolyoxotungstate anion in ionic liquids. *Journal of Electroanalytical Chemistry* 567(1):77-84.
10. López X, Maestre JM, Bo C, & Poblet J-M (2001) Electronic Properties of Polyoxometalates: A DFT Study of α/β-[XM12O40]n- Relative Stability (M = W, Mo and X a Main Group Element). *Journal of the American Chemical Society* 123(39):9571-9576.
11. Rogers EI, *et al.* (2008) Voltammetric Characterization of the Ferrocene|Ferrocenium and Cobaltocenium|Cobaltocene Redox Couples in RTILs. *The Journal of Physical Chemistry C* 112(7):2729-2735.
12. Fedorov MV & Kornyshev AA (2008) Ionic Liquid Near a Charged Wall: Structure and Capacitance of Electrical Double Layer. *The Journal of Physical Chemistry B* 112(38):11868-11872.
13. Kornyshev AA (2007) Double-Layer in Ionic Liquids: Paradigm Change? *The Journal of Physical Chemistry B* 111(20):5545-5557.
14. Lockett V, Horne M, Sedev R, Rodopoulos T, & Ralston J (2010) Differential capacitance of the double layer at the electrode/ionic liquids interface. *Physical Chemistry Chemical Physics* 12(39):12499-12512.
15. Lasia A (2002) Electrochemical impedance spectroscopy and its applications. *Modern aspects of electrochemistry*, (Springer), pp 143-248.
16. Sel O, *et al.* (2013) Determination of the Diffusion Coefficient of Protons in Nafion Thin Films by ac-Electrogravimetry. *Langmuir* 29(45):13655-13660.